NPS ARCHIVE
1968
CARTER, T.

ION SOURCES FOR THE PRODUCTION OF LOW ENERGY BEAMS

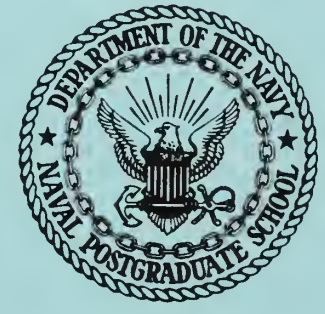
by

Thomas Lee Carter

DUDLEY KNOX LIBRARY
NAVAL POSTGRADUATE SCHOOL
MONTEREY CA 93943-5101

Gaylord
SHELF BINDER
Syracuse, N. Y.
Stockton, Calif.

UNITED STATES
NAVAL POSTGRADUATE SCHOOL



THESIS

ION SOURCES FOR THE
PRODUCTION OF LOW ENERGY BEAMS

by

Thomas Lee Carter

June 1968

[redacted]

[redacted]

ION SOURCES FOR THE PRODUCTION OF LOW ENERGY BEAMS

by

Thomas Lee Carter
Captain, United States Marine Corps
B.S., United States Naval Academy, 1962

Submitted in partial fulfillment of the
requirements for the degree of

MASTER OF SCIENCE IN PHYSICS

from the

NAVAL POSTGRADUATE SCHOOL

June 1968

968
CARTER, T.

ABSTRACT

Three ion sources for the production of low energy ($E < 500$ eV) ion beams have been constructed and tested for use in atomic scattering experiments. Design parameters are given for construction and operation of the sources. Two gas sources, a duoplasmatron and an electron impact source, are capable of delivering beams of H^+, H_2^+, H_3^+, He^+, N^+, and N_2^+, as well as other gas-derived ions, with beam intensities measured at a detector 75 cm downstream of $\sim 0.2\ \mu a/cm^2$. Beam currents closely parallel Langmuir-Child ($I \sim E^{3/2}$) space charge limited intensities. For the duoplasmatron, a full-width energy dispersion of 2-3% of the beam energy is observed. With hydrogen gas, beam composition of 34% H^+, 42% H_2^+, and 24% H_3^+ was achieved. Both gas sources require externally heated cathodes. The third source is a thermal device which produces lithium ion beams of $\sim 0.1\ \mu a/cm^2$ at a detector 75 cm away. The beam energy spread is a few tenths of an eV.

DUDLEY KNOX LIBRARY
NAVAL POSTGRADUATE SCHOOL
MONTEREY CA 93943-5101

TABLE OF CONTENTS

		Page
List of Figures		5
List of Tables		6
List of Symbols		7
Acknowledgements		8
I	Introduction	9
II	General Description of Ion Sources	11
	Common Source Characteristics	11
	Gas Ion Sources	11
	Thermal Ion Sources	12
III	Duoplasmatron Gas Ion Source	14
	Experimental Apparatus	14
	Description of the Duoplasmatron	14
	Duoplasmatron Circuitry	21
	Support Equipment	23
	Operating Procedure	26
	Nature of the Arc Discharge	28
	Cathode Electron Emission	33
	Extraction of the Ion Beam	34
	Experimental Results	40
	Beam Intensity	40
	Lens Configuration	40
	Z. E. Offset	43
	Arc Current	45
	Source Gas Pressure	47
	Mass Analysis and Magnetic Field Effects	50

		Page
	Energy Analysis	52
IV	Electron Impact Gas Ion Source	56
	Source Construction	56
	Operating Characteristics	61
	Source Operation	68
V	Lithium Ion Source	69
	Ion Emitter and Source Construction	69
	Operating Characteristics	70
	Source Operation	71
VI	Discussion	79
	Gas Ion Sources	79
	Ionization Efficiency	79
	Gas Consumption	81
	Cathode Life	83
	Minor Maintenance	84
	Lithium Ion Source	84
Bibliography		90
Appendix A	Theory of Ionization and Gaseous Discharge Pertinent to Ion Source Operation	92
Appendix B	Oxide-Coated Cathode Electron Emission	98
Appendix C	Space Charge Theory	102
Appendix D	Energy Analysis	106
Initial Distribution List		111
DD Form 1473		113

LIST OF FIGURES

FIGURE		Page
1.	Schematic of DETECTOR with Ion Source	17
2.	Duoplasmatron	18
3.	External View of Duoplasmatron	19
4.	Duoplasmatron Mounted in DETECTOR	20
5.	Circuit Diagram for Duoplasmatron	22
6.	Duoplasmatron Support Equipment	25
7.	Properties of a Hot Cathode Arc Discharge	32
8.	Critical Region of Duoplasmatron	38
9.	Plasma Cross-section and Magnetic Field in the Z.E. -Anode Gap	39
10.	Space Charge Limitation - Duoplasmatron	41
11.	Relative Beam Current vs. Z.E. Offset	44
12.	Relative Beam Current vs. Arc Current	46
13.	Beam Current vs. Source Pressure	49
14.	Beam Composition vs. Magnet Current	51
15.	Energy Analyzer Current vs. Beam Energy	54
16.	Energy Dispersion vs. Beam Energy	55
17.	Beam Energy Calibration Curve	55
18.	Electron Impact Gas Ion Source	58
19.	External View of Ion Source	59
20.	Circuitry Schematic of Electron Impact Ion Source	60
21.	Grid Current vs. Grid Voltage	65
22.	Grid Current vs. Source Pressure	65
23.	Total Hydrogen Beam Intensity vs. Source Pressure	66
24.	Beam Current vs. Source Pressure, Hydrogen Species	66

Page

25. Nitrogen Ion Current vs. Source Pressure 67

26. Total Hydrogen Beam Instensity vs. Grid Voltage 67

27. Lithium Ion Emitter 73

28. Lithium Ion Source 74

29. External View of Lithium Ion Source 75

30. Lithium Source Emission 76

31. Lithium Source Mass Analysis 77

32. Diode Emission Characteristic of Li^+ Emitter 78

33. Variation of Potential Between Parallel Plate Electrodes Showing Effect of Initial Velocity of Emission 86

34. Electrical Discharges in Gases 93

35. Analyzer Energy Spread vs. Beam Energy Showing Transmission Function and Li^+ Data 109

36. Method of Graphically Obtaining $I(E')=\int_0^\infty T(E-E')F(E)dE$ 110

LIST OF TABLES

TABLE

I Comparison of Ion Sources 89

LIST OF SYMBOLS

D	Z.E.-anode coaxial offset (cm)
E	nominal ion beam energy (eV)
ΔE	full-width at half maximum beam energy dispersion (eV)
I	non-specific current (amps)
j_e	electron current density (amps/cm^2)
j_+	ion current density (amps/cm^2)
ℓ	particle path distance between collisions (cm)
m	electron mass (gm)
M	ionic mass (gm)
P	pressure (torr)
r	unspecified radius (cm)
s_e	ionization efficiency (ion pairs/electron cm @ P=1 torr)
$T(E-E')$	energy analyzer transmission function (eV)
T_e	electron temperature (^oK)
T_g	gas temperature (^oK)
V_a	anode fall (volts)
V_c	cathode fall (volts)
V_i	ionization potential (volts)
V_g	grid voltage (volts)
V_s	discharge breakdown voltage (volts)
α	first Townsend discharge coefficient (ion pairs/electron cm)
γ	total secondary emission coefficient (electrons/ion)
ρ_{net}	net charge density (cm^{-3})
ρ_e	electron charge density (electrons/cm^3)
ρ_+	ion charge density (ions/cm^3)
λ	mean free path (cm)

ACKNOWLEDGEMENTS

The author wishes to express his gratitude to Dr. Otto Heinz, the supervisor of this work, whose interest and whose assistance have contributed greatly to its development. Additionally the advice of Dr. Charles Cook, Dr. William Aberth, and Dr. J.R. Peterson of the Stanford Research Institute is gratefully acknowledged.

Much of the research for this effort was carried out by former officer-students at the Naval Postgraduate School and Dr. Heinz. I am most grateful to Dr. Heinz, Lt. Thomas O. Bush, LCDR George H. Strohsahl, and LCDR H.B. Haskell for their considerable contributions.

My special thanks go to Mr. Thomas Maris of the technical staff of the School who constructed the ion sources which are the basis of this project.

CHAPTER I

INTRODUCTION

Ion sources are an essential component in all heavy particle accelerators and similar devices. A great deal of effort has gone into the development of ion sources of all kinds over a period of more than half a century and an extensive collection of literature is available on all aspects ion source research. However, most of this work was done with a view toward high energy accelerators, where typical ion beams have energies of many kilovolts when extracted from the source.

The research reported in this paper is concerned with ion sources used in low energy ($E < 500$ eV) ion beam experiments where phenomena of space charge and energy dispersion become critical. The three sources discussed in this thesis were tested and used over a period of three years with the participation of several Naval Postgraduate School students. New experimental results on the use of the duoplasmatron source at low energies are shown. The plasma of the duoplasmatron is generated by electron impact on gases. The advantage of this source is the two-fold (hence, "duo") constriction imposed upon the plasma by a magnetic field and the source geometry. Plasma confinement greatly enhances the ion beam intensity derived while keeping the gas flow from the source to a minimum.

In addition, a catalogued summary of earlier and current work done in this laboratory on two other types of low energy sources is presented: an electron impact source for use with gases and a thermal source for the production of lithium ion beams.

The experimental results, hardware and operating characteristics are discussed for each source separately while some of the underlying theory such as thermionic emission, gas discharge theory, etc., is treated in appendices. While the primary concern remains the production of the most intense beam possible, many other questions such as energy spread, beam composition and gas load on the system must also be taken into account in evaluating the performance of each source.

CHAPTER II

GENERAL DESCRIPTION OF ION SOURCES

I. COMMON SOURCE CHARACTERISTICS

The basis of operation of the three ion sources investigated is the creation of ions in a region of positive potential and their acceleration to ground potential with a resultant kinetic energy corresponding to the potential change. The extraction lens in each case is grounded, and the ion beam kinetic energy is essentially the potential of the ion source. Subject to the limitations of space charge and lens aberration effects, extraction and focusing of the beam is achieved with the einzel lens particular to each source so as to maximize the ion flux downstream.

II. GAS ION SOURCES

The earliest types of gas ion source employed an ordinary glow discharge. Ions formed in such a source, however, have an energy dependence upon their place of origin in the discharge, hence ion energy differences on the order of magnitude of the potential drop within the positive column (see Appendix B) can exist. More recent sources employ a low voltage arc to avert this problem.

In the conventional arrangement of a gas ion source, a potential of the order of 100 volts attracts electrons from a hot filament to an anode, a process which ionizes the intermediate gas by means of inelastic collisions, and creates a plasma. An aperture in the anode allows the plasma to escape from the arc chamber and ions can then be extracted by the application of electrostatic fields. The operating pressure for a low voltage arc is of the order of 10^{-1} to 10^{-3} torr, considerably lower than that of a glow

discharge, and arc potentials are normally less than 100 volts. Ion densities, by virture of the plasma, are particularly high in the vicinity of the anode aperture, and high beam intensities are obtained with apertures as small as 0.25 mm diameter.

When in contact with a physical boundary, the plasma forms a protective sheath about itself. The sheath, in effect, separates the main body of the plasma from its environment. Unlike the main body, the sheath is not electrically neutral and strong electric fields may be present in it. The thickness is on the order of a Debye length. Due to high ion densities and low arc potentials, the Debye shielding surrounding the cathode is such that nearly the entire arc voltage rise appears within a few mm. of that electrode. The plasma potential remains close to that of the anode, and no appreciable electrostatic fields can be maintained within the plasma.

III. THERMAL ION SOURCES

Thermionic emission of positive and negative ions from coated filaments is a phenomenon which has long been known, and ion sources have operated on this principle for decades. Emission of ions also takes place from metals when heated almost to their melting points. The process is grossly inefficient in that a multitude of neutral atoms are evaporated for each positive ion. However, efficient filament sources of ions of alkali metals have been produced by heating synthetic alkali alumina silicates to around 1100°C. One such source generates lithium ions, and mineral β-eucryptite ($Li_2O:Al_2O_3:2SiO_2$) appears to be the best emitter. Initially

impurity ions represent about one percent of the total ion current, but are further reduced after prolonged operation. The emission holds up fairly well even when most of the initial lithium content of the source has been evaporated. Extraction of the ion beam is similar to that of gas ion sources. The emitter is placed at a positive potential and the ions are accelerated in a beam by placing a grounded probe nearby. In addition to ease of construction and operation, this source also delivers a virtually monoenergetic beam of ions.

CHAPTER III

DUOPLASMATRON GAS ION SOURCE

I. EXPERIMENTAL APPARATUS

Experimentation was performed in two different vacuum chamber assemblies; one, in which active ion beam collision studies are being made, and which includes a mass spectrometer; and another which will be referred to as DETECTOR, a simple vacuum chamber assembly in which a beam detector as well as an electrostatic energy analyzer can be placed. The scattering experiments and equipment are yet to be described, but the DETECTOR chamber, beam detector, energy analyzer, and associated vacuum equipment are fully treated by Strohsahl[1]. Figure 1 shows the salient features of the duoplasmatron mounted in DETECTOR.

II. DESCRIPTION OF THE DUOPLASMATRON

The physical dimensions of the duoplasmatron are in keeping with desired compactness and general adaptability. The device can be used in an assortment of apparati as an ion beam source with no internal or external modification.

The duoplasmatron is shown in Figs. 2-4. The Z-Electrode (Z.E., swischen - intermediate) and filament are mounted coaxially in the magnet coil form so that all the arc-generating components form a rigid unit which can slide across the base flange.

The Z.E., mild steel, is provided with an O-ring groove on the inside face of the base, and a seat for a glass vacuum seal ring. The ring electrically insulates the Z.E. from the magnet coil and anode. Teflon and ceramic rings were tried here: the former deteriorated badly under the intense heat generated at the base of the

Z.E., flaking to the extent that the anode aperture became clogged with carbon-like deposits; the ceramic failed to hold a satisfactory vacuum. The Z.E. aperture is 0.384 cm in diameter.

The filament flange, copper, is held to the base of the Z.E. with four metal screws, and is provided with two ¼" ID gas ports (not shown) and two insulated electrical feed-throughs. The inside face of the flange is finished smooth for O-ring seal. To one gas port stem is fixed a thermocouple vacuum gauge; the other is for gas entry into the duoplasmatron. Gas flow is controlled with a simple needle valve. The filament is held atop two 1 cm high copper stubs stemming from the kovars. Construction of the filament is of a 5.1 x 7.6 cm rectangular piece of 70 x 70 mesh, 0.1140 mm dia. nickel wire cloth, rolled tightly about the long edge and bent into a hairpin shape with no kinks. A Ca-Ba-Sr oxide coating (see Appendix B) of paste consistency is applied by painting or dipping and hardened. The entire volume of the rolled filament is filled, except for 1 cm on each end to make for good electrical contact.

The magnet coil form, cut from a copper block, surrounds the Z.E. and holds the arc-generating components against the base flange. Both metal faces at this juncture are finished extremely smooth for ease of sliding motion relative to one another. The magnet is wound with 1000 turns of #20 copper wire.

The base flange holds the anode, anode insert, and insert clamp, and is electrically insulated from the support flange by a teflon ring. It is likewise fitted with O-ring grooves on either side. The flange, anode, and insert clamp are made of mild steel, the

insert itself being copper and non-magnetic. The aperture is 0.508 mm in diameter and 0.25 mm deep. The anode-Z.E. separation is 0.50 mm.

The focus stack is a three-element einzel lens, discussed further in Section IX of this chapter. It is sufficient here to report that the gap between the anode insert and the extracting lens (L_1) is 0.38 mm. The lens is constructed of aluminum, as are the two pairs of deflecting plates mounted forward of the lens' third element (L_3). The lens and deflectors are held in place by four 20 cm long ceramic insulating rods which stem from the support flange. Electrical connections for all internal components are made through seven feed-throughs in the support flange, and teflon-coated copper wires.

The arc-generating group is secured by a steel top-plate and two metal rods anchored in the support flange. To the base flange are attached four threaded mounts and adjusting screws which control the lateral displacement of the Z.E. axis with respect to the anode aperture. A protective metal hoop is secured externally to the support flange and surrounds the exposed portion of the duoplasmatron. To this is fixed the gas entry needle valve.

The Z.E., magnet coil, and base flange are water cooled in series. Flexible tubing is provided between each element in order to allow for movement of the sliding parts and easy disassembly. Under humid conditions it is important that the cooling system be secured when the ion source is not in operation, as water condensation collects on the metal and glass ring surfaces in the air gap between the Z.E. and magnet coil, shorting out the arc voltage.

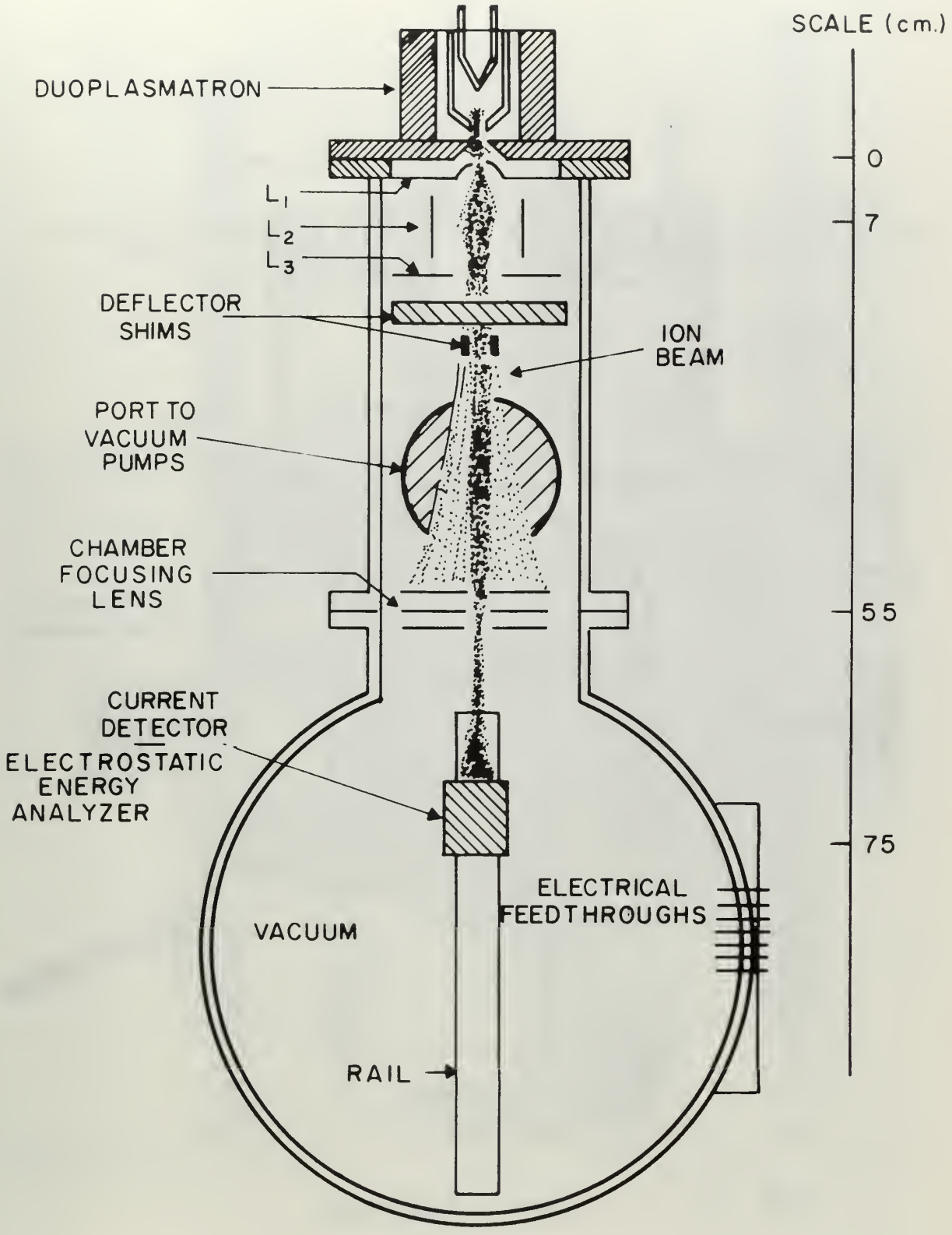


FIGURE 1

SCHEMATIC OF DETECTOR WITH ION SOURCE.

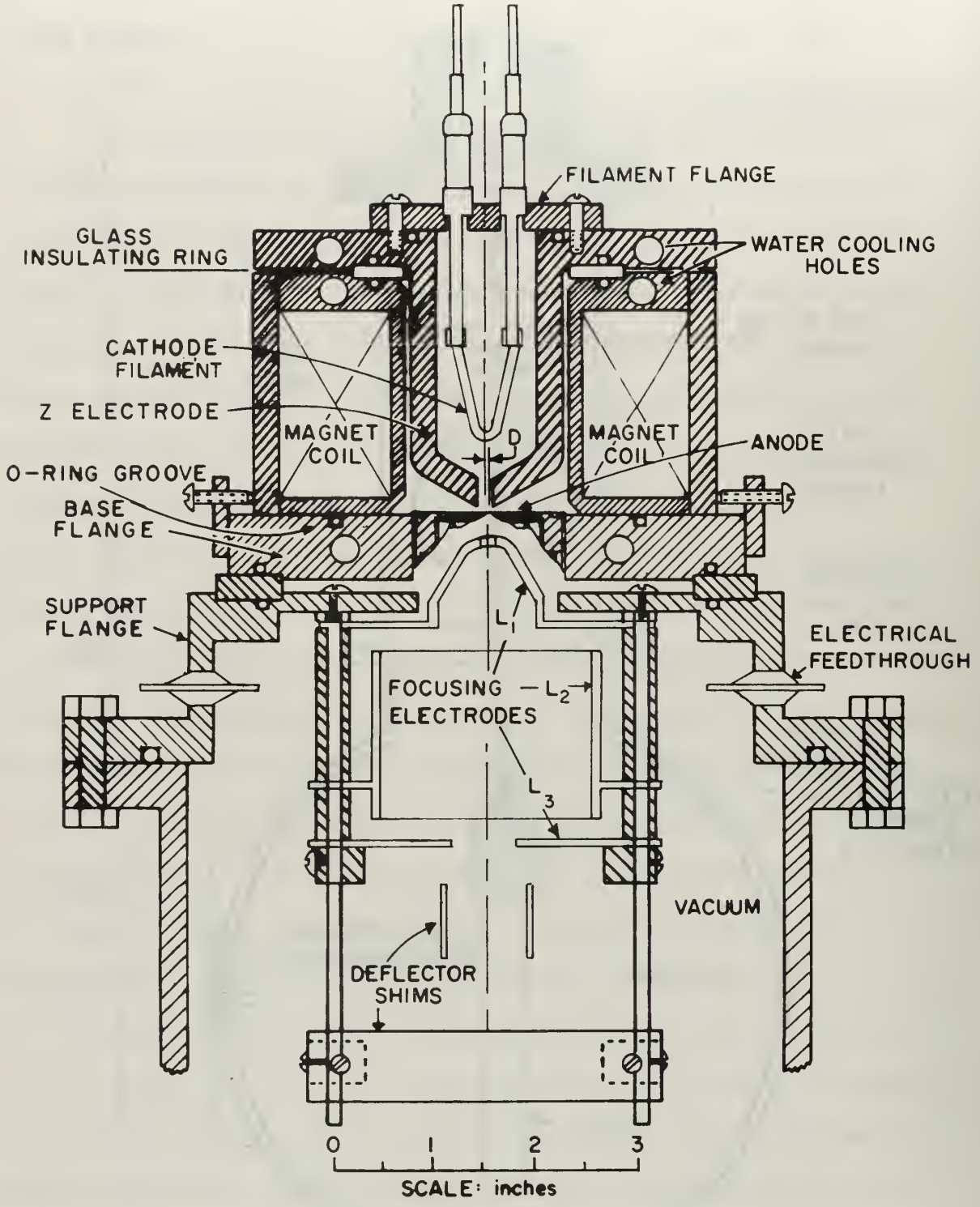


FIG. 2. DUOPLASMATRON

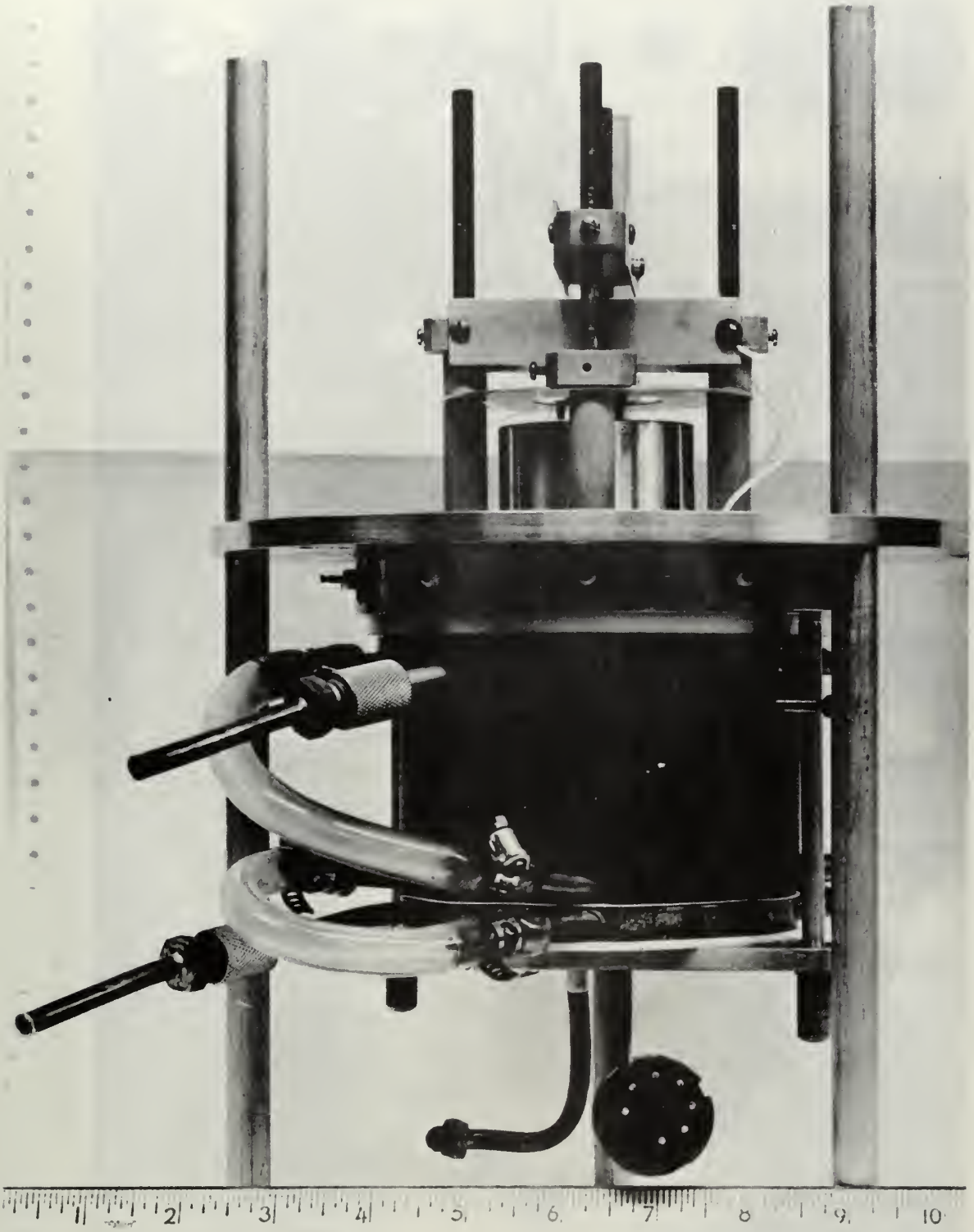


FIG. 3.

EXTERNAL VIEW OF DUOPLASMATRON

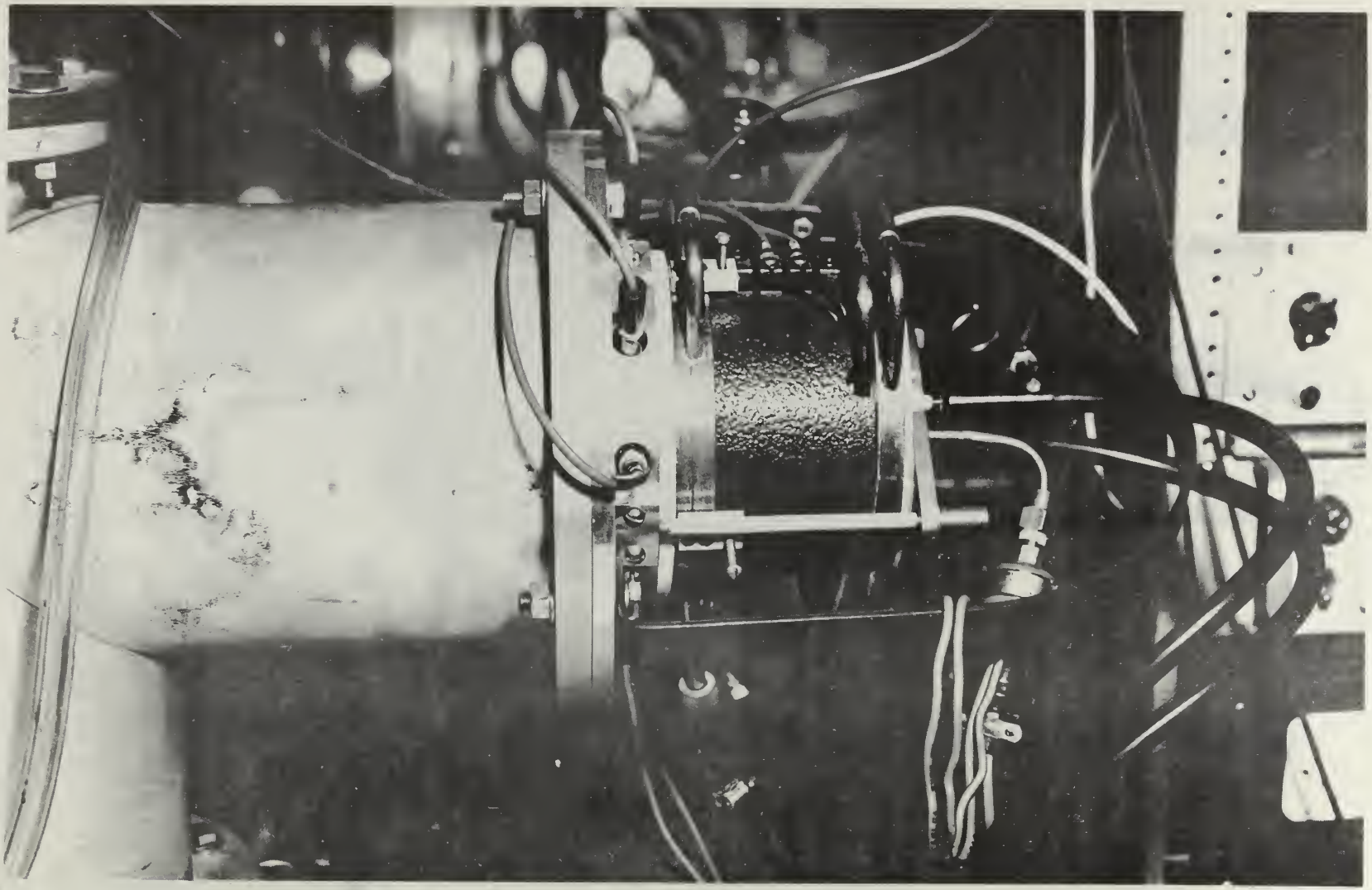


FIG. 4. DUOPLASMATRON MOUNTED IN DETECTOR

III. DUOPLASMATRON CIRCUITRY

A circuit diagram for the arc generating and extracting components of the duoplasmatron is shown in Fig. 5. For gas breakdown, the Z.E. is held at the anode potential (position 1 in diagram); after the arc is established it is switched to that of the filament (position 2). In the operating mode, it is possible to keep the Z.E. slightly more positive than the filament by inserting an additional resistance between the Z.E. and the filament. This option has not been tried.

With water flowing in the cooling jacket, the Z.E. -anode resistance falls to 10K, which accounts for a small fraction of an amp in the indicated arc current. The current leak seems to have no detrimental effect.

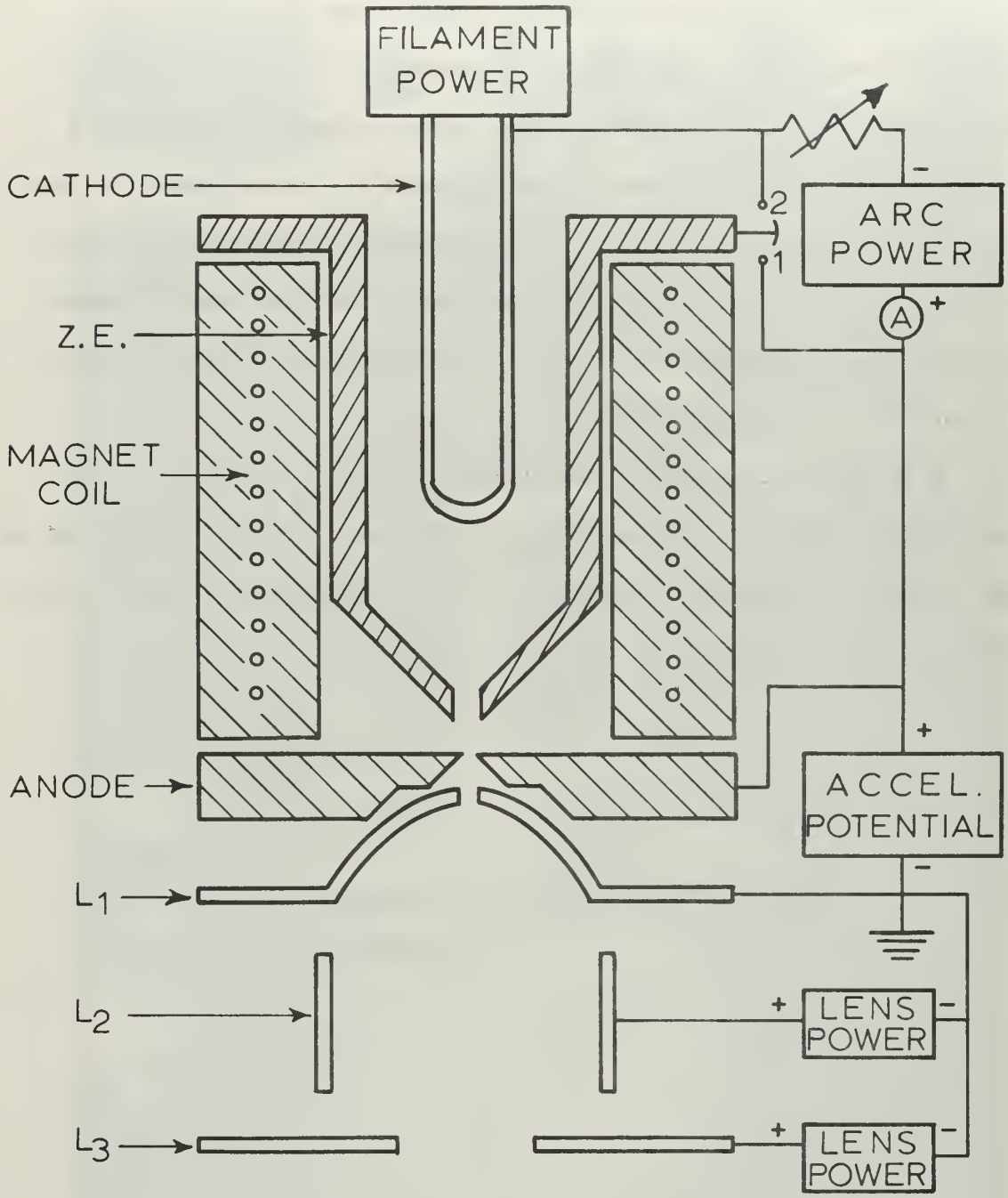


FIG. 5.

CIRCUIT DIAGRAM FOR DUOPLASMATRON

IV. SUPPORT EQUIPMENT

The support equipment for the duoplasmatron is pictured in Fig. 6. The rack carries power supplies for the filament, arc generation, magnet, and focus stack.

The filament is powered by a 25 amp AC, powerstat controlled transformer. The filament leads are heavy duty 30 amp cables. The arc voltage supply is a Kepco model KR-19M, 300-500 v., 1.5 amp DC, voltage regulated power supply with a variable (up to 375 ohms) resistor inserted externally in series. Upon initiation, arc resistance can fall to extremely low values and the power supply is insulated from excessive current by the resistor. The resistance is kept as high as possible consistent with a given arc current in order to absorb occasional surges.

The accelerating voltage is provided by an Electronics Measurements Co., voltage regulated power supply, model 204-A, 0-500 v., 0-500 ma DC. The ion beam occasionally causes arcing between the anode and the probe (L_1) to intermittant values of 25 ma maximum. The magnet current is furnished by a solid state, Power Designs 0-36 v., 0-5 amps DC, package. This supply features a fine adjust control which is essential for peaking beam currents.

There are four elements of the focus stack which require power: L_2, L_3, and the two pairs of deflecting plates. The lenses draw a fair amount of current and call for high, adjustable voltages, hence batteries are supplanted by two Harrison 6515A DC power supplies, 0-1500 volts. The deflection plates are operated with one 45 volt battery each, and wired to permit polarity reversal

with one plate always held at ground, the other at some positive potential.

In DETECTOR use, the chamber focusing lens is monitored from the same console as the einzel lens, and requires two 300 volt batteries.

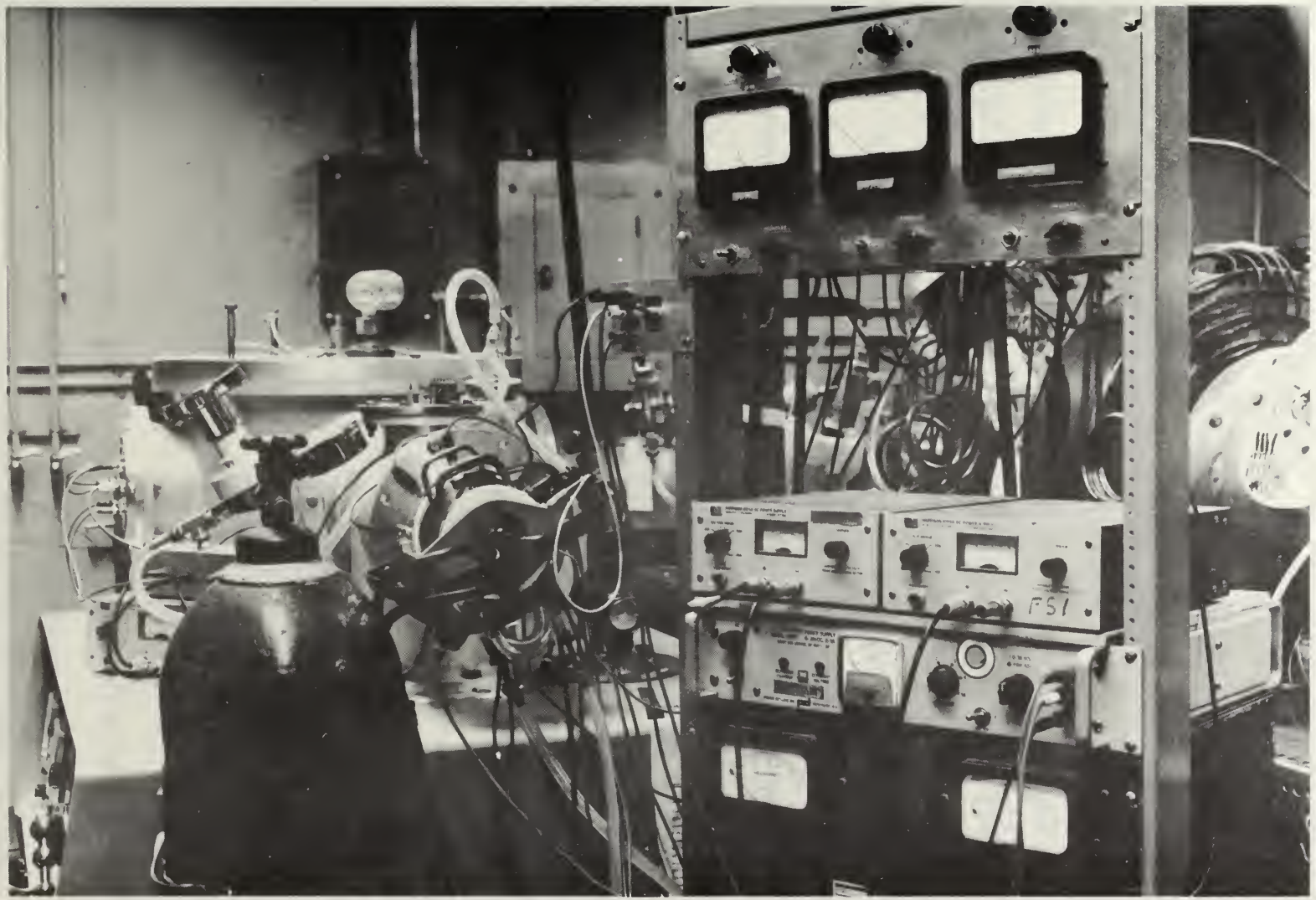


FIG. 6. DUOPLASMATRON SUPPORT EQUIPMENT

V. OPERATING PROCEDURE

Operating procedure for the duoplasmatron is outlined as follows:

(i) Establish gas pressure of about 0.2 torr using the thermocouple gauge. Secure the gauge before striking the arc. Gas is passed through liquid nitrogen trap prior to entry into the source to remove water vapor.

(ii) Start water cooling. Warm up all components. Set filament current to 5 amps for 5 minutes, then raise to operating value of 10 amps. This corresponds to a power consumption of 11 watts, and provides adequate electron emission for both initiation and maintenance of the arc.

(iii) In the start position (see Fig. 5), raise arc voltage until discharge appears. Arc current of 0.1 amps is sufficient. Keep series resistance at maximum; reduce resistance if arc fails to initiate.

(iv) Switch to operate position (Fig. 5) and monitor arc voltage until steady arc current at the desired level is reached (0.3-1.0 amps). Increase series resistance to maximum value which will accomodate arc requirement. Initially the current may be unsteady; allow several minutes to stabilize.

(v) Set accelerating voltage. If arcing occurs between the anode and L_1, reduce voltage and increase slowly.

(vi) Adjust focus and deflector potentials to maximize beam at detector. Adjust magnet current to peak beam. Refocus.

(vii) Refocus beam and reset magnet current for each accelerating voltage used.

VI. NATURE OF THE ARC DISCHARGE

There are several classifications of arc discharges, but the natural division lies between those which feature copious electron emission from "cold cathodes" and are self-maintaining, and those which are non-self sustaining and require externally heated filaments. In the duoplasmatron self-maintaining arcs have been observed for as long as three hours duration, indicating that the arc operates in a borderline area between a Townsend discharge T_2 region (see Appendix A) and the self-maintaining domain.

The principle features of a low pressure arc with an external emission source are the cathode fall and the plasma (see Fig. 7). The cathode fall, V_c, is the potential drop across the space through which electrons travel before they produce gas ionization, or more generally, the region in which electrons acquire ionization energy. The plasma of a discharge is that quarter in which the concentration of positive ions equals that of electrons, negative ions assumed absent. It is a region of very dense equal space charges which appears instead of the positive column associated with glow discharges. The plasma shows very small losses, and is essentially unipotential. The voltage drop across the discharge is due almost entirely to the cathode fall. Electron emission in cold cathode arcs is dependent upon filament bombardment by high energy ions as well as intense electric fields produced by positive space charge near the cathode. Total electron emission from an externally heated filament is relatively independent of incoming ion energy, and discharges can occur with smaller electric fields than

in the self-maintaining case. Hence V_c is lower in the duoplasmatron than for cold cathode sources. The cathode fall varies between 50-80 volts with hydrogen gas at a source pressure in the region of 0.2 torr.

As shown by Fig. 7a, the cathode fall space is characterized by two regions of opposite space charge and a neutral zone. At the cathode a negative space charge is established due to primary electron emission. A positive space charge exists in front of the plasma body due to repulsion of plasma electrons by the cathode. Near the midpoint in the cathode fall, space charge is equalized and an electrically neutral region created. Charge density is pictured in Fig. 7c; it is estimated that the maximum values of $\rho_{net} = \rho_+ - \rho_e \approx 10^{-4}\, \rho_e \approx 10^{-4}\, \rho_+$. The electric field between the two space charge regions is responsible for the cathode fall voltage.

The anode phenomena of low pressure arcs are essentially those of a glow discharge, with the anode fall $V_a \ll V_c$. Anode fall appears because a negative space charge sheath develops between the anode and the plasma. Near the perimeter of the plasma higher electron mobility causes the lighter particles to diffuse outward at a greater rate than ions. Electron attraction and ion repulsion with respect to the positive anode accelerates this process. The negative particles impact on the anode but ultimately create a space charge great enough to retard further escape of electrons. In doing so, the plasma is insulated from losses to the electrode, and an electric field is established between the net positive plasma and the negative envelope which surrounds it. The electric field points away from the plasma, raising the plasma potential above that of the anode surface.

By calculation of the space charge limited current for ions and electrons moving simultaneously into and out of the cathode, we find

$$\frac{j_e}{j_+} = \left(\frac{M}{m}\right)^{\frac{1}{2}} \qquad \text{(III.1)}$$

For electrons and protons, equation (III.1) gives $j_e/j_+ \approx 42$. In a contained H^+ arc there must be one ion pair produced for every 42 electrons emitted from the cathode. With the incorporation of plasma losses such as in the ion beam of the duoplasmatron, this figure must be much higher.

The temperature variation of an arc discharge is shown in Fig. 7d. Since neutrals are present in the arc along with electrons and ions, gas temperature is only slightly above the ambient temperature. Electron temperature is much higher. Both T_g and T_e are position dependent, causing the core of the arc to be considerably hotter than the outside region.

Though the plasma is considered to be everywhere unipotential, an isotropic Maxwellian energy distribution is established in part by a variety of interactions which take place. Primary electrons arrive at the plasma boundary with nearly uniform energy. Occurring within the plasma are ionizations, excitations, electron interactions, collisions between excited atoms, etc. Many electrons gain energies in excess of the ionization potential of the neutral gas. Small concentration gradients arising from the drift velocity of the plasma out the Z.E. aperture are an additional perturbation

peculiar to the duoplasmatron. The result is the conversion of a narrow electron energy spread (< 1 eV) into a fairly wide (~ 3 eV) ion energy dispersion, an exceedingly complex process, beyond the scope of this paper.

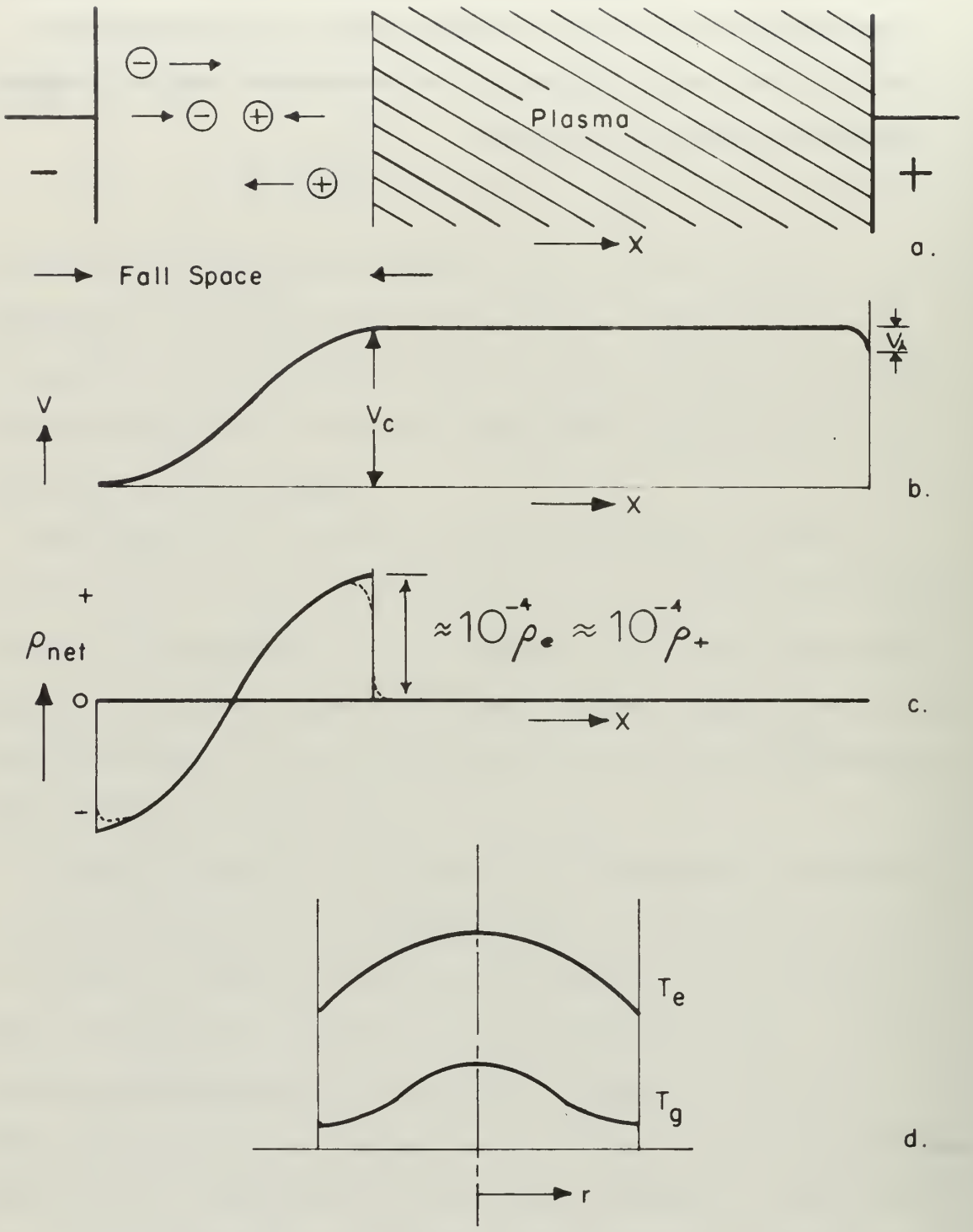


FIG. 7.
PROPERTIES OF A HOT
CATHODE ARC DISCHARGE.

VII. CATHODE ELECTRON EMISSION

It is the copious emission of electrons by the cathode of the duoplasmatron which, at operating pressures, allows an arc discharge to take place within the Z.E. vice a high-voltage glow discharge. The high electron flux causes sufficient gas ionizations to generate a plasma characterized by the very low cathode fall (50-80 volts) discussed in Section VI of this chapter. The source of electron emission is a metal (Ba, Ca, Sr) oxide coating applied to the filament, which when heated produces atomically neutral metal atoms at the surface of the cathode. The monatomic layer formed has a particularly low work function (1.2 volts) and electrons are thermally emitted at relatively low temperatures (700^{o}C). A low filament power consumption follows (11 watts). Higher power (30 watts) was initially used and resulted in filament burnout. The operating value is that which will suffice both to initiate and maintain the arc, and extends cathode life to more than 100 hours. Appendix B treats electron emission from oxide-coated cathodes in detail.

VIII. EXTRACTION OF THE ION BEAM

The plasma and extraction geometry are shown in Fig. 8. The plasma envelope is caused to draw down to a very small cone inside the Z.E. by the concave shape of the forward end of the electrode. The Z.E. aperture acts as a plasma leak; any effort to force plasma through the aperture would cause ions and electrons to be separated, and reduce the beam current. The amount of gas and plasma escaping from the discharge chamber, the size of the aperture, and the available current of a non-space-charge-limited beam are closely related. As long as the ion beam is space charge limited, arc current and gas pressure changes do not proportionally alter the beam intensity, but serve only to change the shape and density of the emitting space charge surface. The behavior of beam current with arc current is shown in Fig. 12. Variation of beam intensity with source pressure is normally more significant, and is discussed in Section IX of this chapter.

An important factor in determining plasma density is the electron density in the discharge. Trapping electrons in the arc results in effective utilization of primary cathode emission, and is responsible in part for the high ionization efficiency of the duoplasmatron.

Within a plasma only negligible potential gradients are permissible, while much larger potential gradients can be maintained at plasma-electrode interfaces. The plasma generally takes a uniform potential very near that of the most positive electrode in its vicinity, the anode in this case. The Z.E. is therefore at a

potential lower by an amount equal to the arc voltage, and acts as an electron reflector. Electrons in the discharge chamber are trapped in the arc until they either acquire enough energy to transit the Z.E. plasma sheath or filter through to the anode region. Those electrons which do reach the Z.E. from the plasma are not a total loss, due to emission of low-energy secondary electrons from the Z.E. surface which can become trapped in the arc. The longer electrons remain in the path of escaping gas, the greater ionization efficiency they have.

The plasma formed in the arc chamber is physically constricted by the conical shape of the Z.E., and drifts into the open region between the Z.E. aperture and the anode. Here the cross-sectional area of the plasma is essentially determined by radial diffusion and recombination of electrons and ions in the outer zone of gas. Radial diffusion can be reduced by applying a longitudinal magnetic field in the gap, imposing a second, partial constraint on the plasma. The magnetic field forces electrons into tighter cyclotron orbits than the heavier ions, causing the former to diffuse radially outward less rapidly than the positive particles, and creating a slight ion/electron gradient. This promotes an outer ion sheath and an inner electron core. The plasma cross section takes on the appearance shown in Fig. 9, where $\rho_{net} \ll \rho_e \approx \rho_+$. Throughout the cross section, because electron losses from the plasma are slowed, the ionization frequency necessary to maintain a steady state discharge is less.

The ferromagnetic properties of the Z.E. and anode come to bear by shielding the arc chamber and concentrating the magnetic field in the two-electrode gap (see Fig. 9). The plasma continues to move through the anode aperture and forms a concave sheath in the face of the anode insert, where the same magnetic constraints on electron and ion motion are applied.

The anode fall region, anode, and grounded probe (L_1) form the ion beam extraction system. For the plasma to pass through the anode aperture it must traverse the negative space charge sheath of the anode fall (V_a not accurately known, but estimated to be 4-10 v). The gross effect is for the plasma to carry through, but on an atomic scale the electrons tend to be retarded and the ions tend to be accelerated. The space charge sheath is non-uniform due to physical offset of the aperture itself (D in Fig. 9), so that the amount of acceleration that an ion undergoes is not constant. It can reach the anode face with up to 10 eV energy. Positive ions in this way are extracted from the Z.E. -anode region with an energy distribution, which probably accounts for some of the measured ion beam energy spread.

Once in the anode face, the electric field causes the surface of the plasma to retreat from the probe until the space charge of ions leaving the plasma cancels the field at the surface. The boundary between the positive space charge and the dense plasma forms the surface from which the ion beam originates. At low beam energies the plasma extends further into the accelerating region than when higher potentials are used. At increased voltages the

plasma withdraws toward the anode face and the positive space charge layer simultaneously thickens. The curvature of the emitting surface and crude focus of the beam are altered.

A notable characteristic of the duoplasmatron is the loss of ions from the plasma to the Z.E. by reverse extraction. The anode-Z.E. geometry forms an accelerating system much like the anode-probe. The plasma spreads out on the rear anode surface and behaves similar to that in the anode face; an ion current is propelled to the Z.E. The loss is surely one of efficiency, but probably does not effect the intensity of the forward beam.

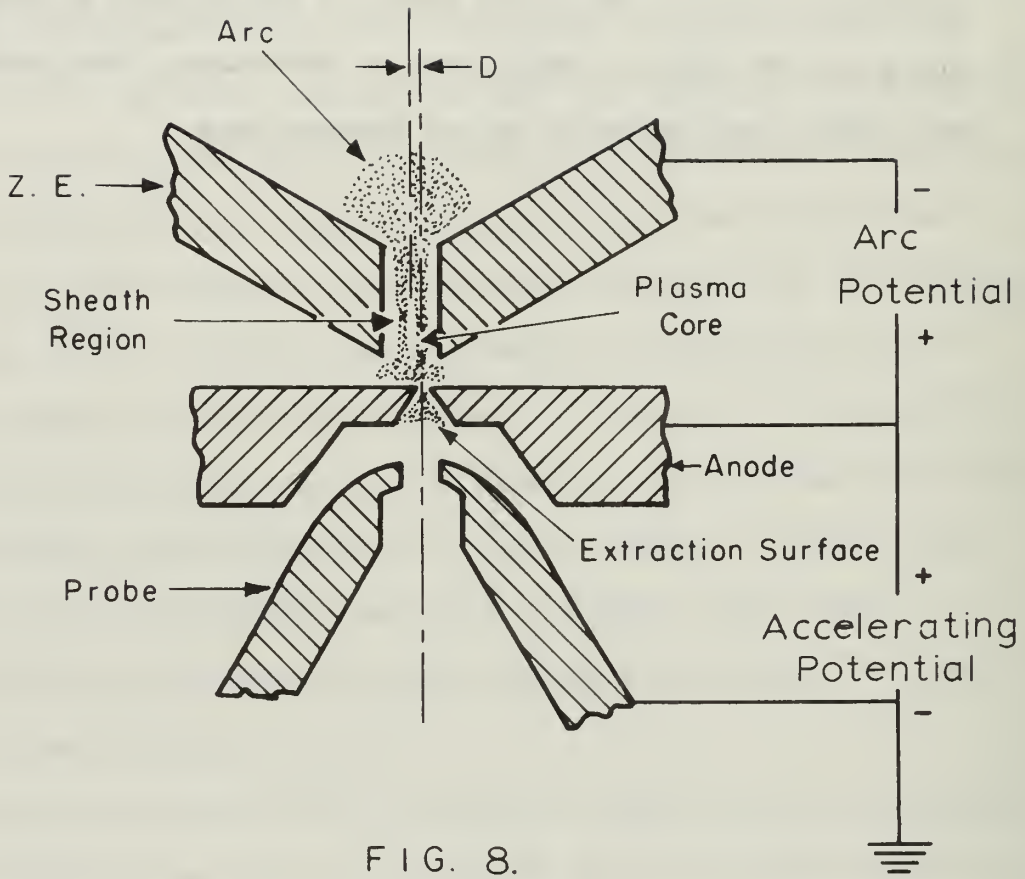


FIG. 8.

CRITICAL REGION OF
DUOPLASMATRON.

EXPANDED
PLASMA CROSS SECTION

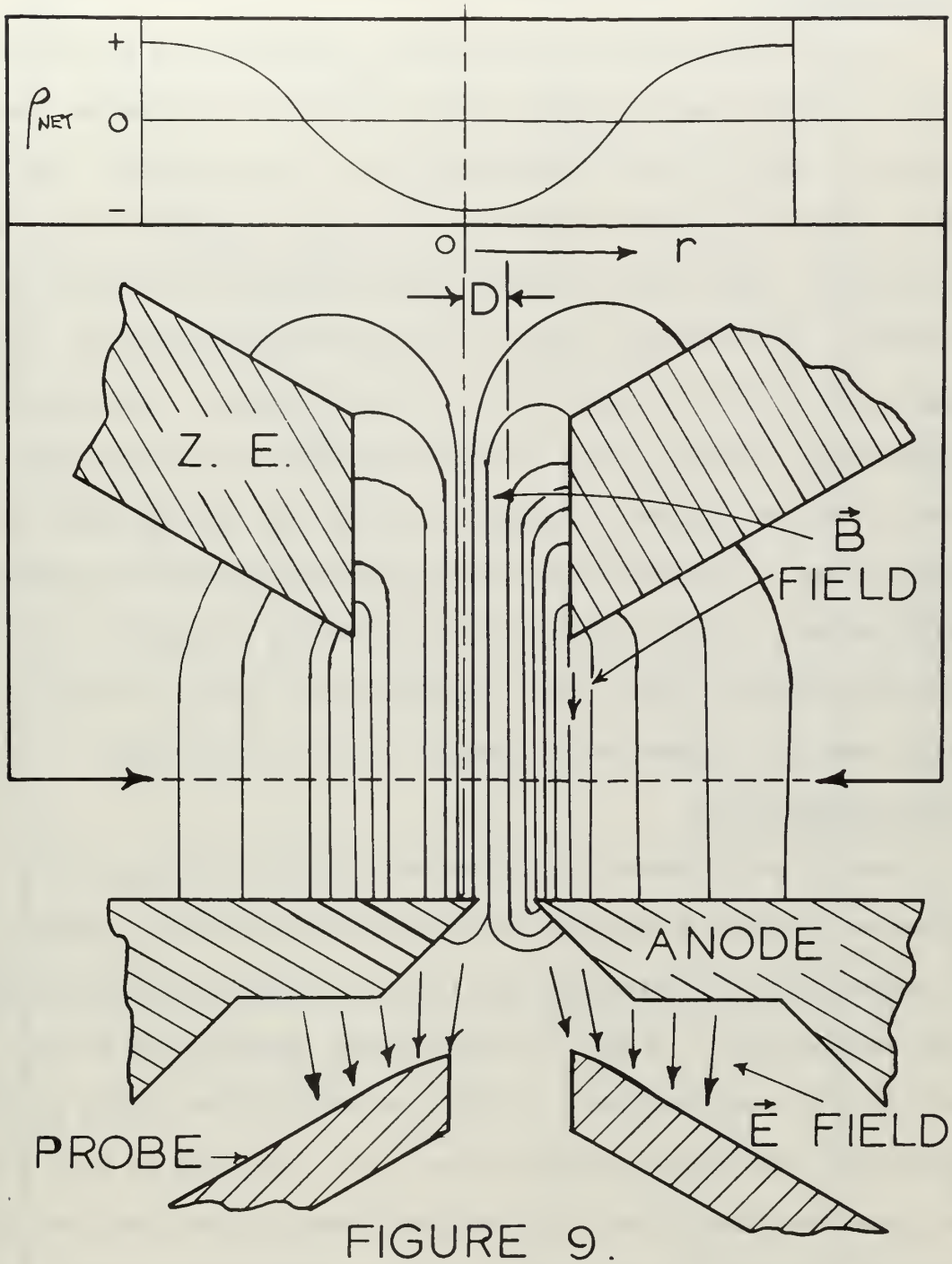


FIGURE 9.

PLASMA CROSS SECTION AND MAGNETIC FIELD IN THE Z.E.-ANODE GAP

IX. EXPERIMENTAL RESULTS

Beam Intensity

The principle aim in building and investigating the duoplasmatron ion source was to obtain high density H^+ ion beams at low beam energies. Early in the experimentation it was seen that the beam which could be developed compared closely in magnitude with the theoretical space charge limited beam which can be produced in our geometry. Space charge theory is discussed in Appendix C, and a sample calculation is done by way of illustration. Elaboration of the example is made in Fig. 10, in which the theoretical space charge limited current is computed for H^+, H_2^+, and H_3^+ beams at energies up to 1 keV for the duoplasmatron/DETECTOR arrangement. Measured beam intensities up to 500 eV energy produced by the ion source are of the same order of magnitude as those pictured. Measurements at higher beam energies have not been made.

Lens Configuration

During experimentation the effect upon beam intensity of numerous parameters peculiar to the duoplasmatron was explored. As a prelude, the configuration and potentials applied to the einzel lens were studied. A lens of three plane elements was tried, varying the aperture sizes, as well as combinations using both plane electrodes and the cylindrical lens (L_2). Pictured in Fig. 2 is the final configuration; the remainder tested gave from poor to slightly inferior performance. At best, focusing increases ion beam intensity by a factor of ~ 2 over the space charge limited beam. Normally, the potential placed on L_2 is positive and approximately equal to the beam energy. That placed on L_3 is variable,

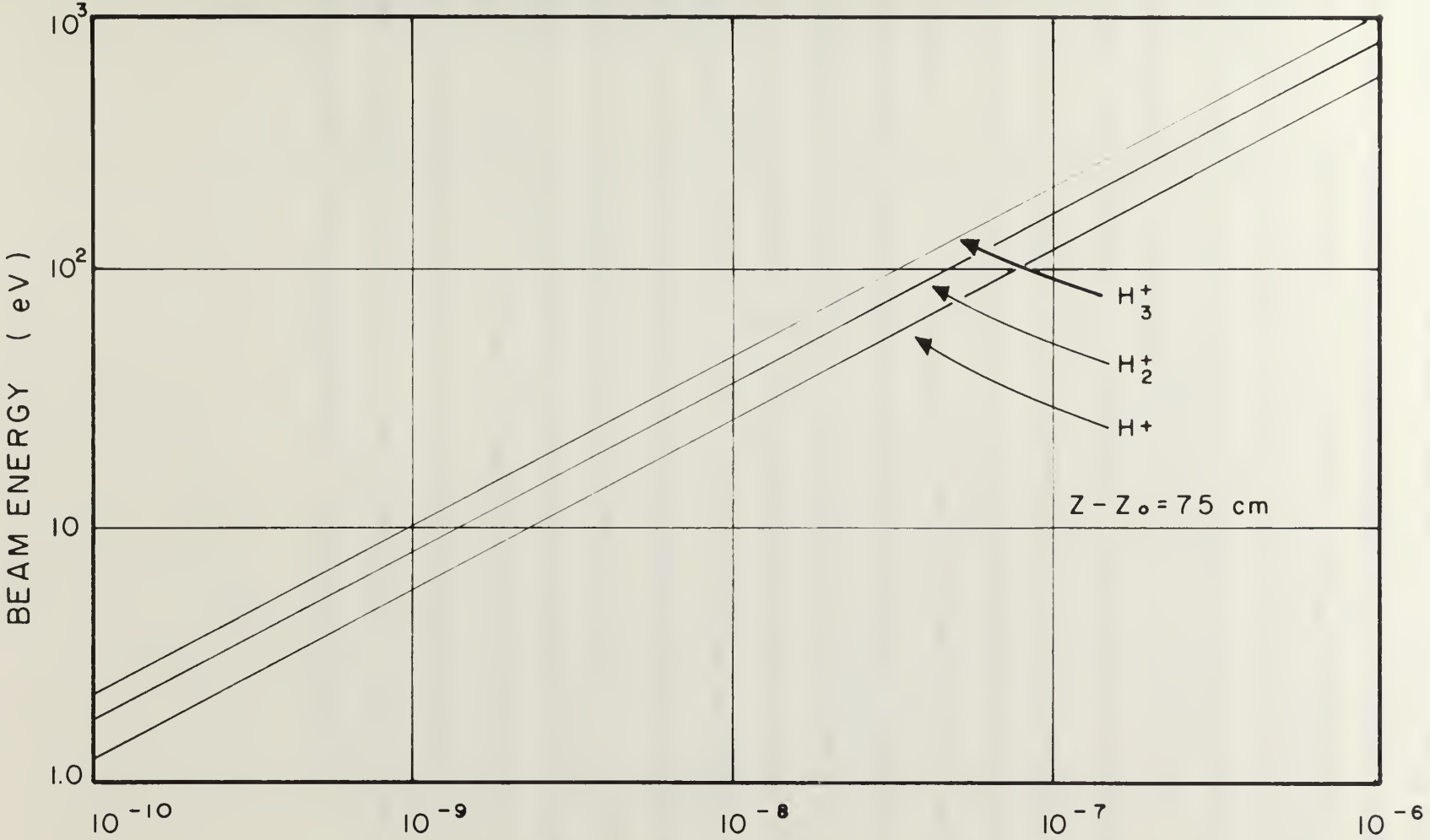


FIG. 10. SPACE CHARGE LIMITATION — DUOPLASMATRON.

ranging from -100 v. at low beam energies to +150 v. at a beam energy of 500 eV. L_3 is held at ground potential for beam energy in the 200-250 eV region.

Z.E. Offset

Aberth and Peterson[2] describe negative ion current measurements with their duoplasmatron as a function of Z.E. displacement from the anode axis (D in Figs. 8 and 9), and indicate that maximum values of current are produced as D exceeds the anode aperture diameter, before falling off gradually with increasing D. Lawrence[3] reports like findings in negative ion beam studies at Los Alamos.

This experimentor found similar behavior for positive hydrogen and helium ions produced in the duoplasmatron only above beam energies of 250 eV. The suggested explanation is that ions are formed in the cooler region outside the hot inner electron core of the plasma. Concurrently, by virture of the magnetic field, the net charge density of the plasma cross section grows slightly positive with increasing radius from the plasma core (Fig. 9), and this increased potential drop between the plasma and anode may enhance the ion current through the emission hole. Above beam energies of 250 eV maximum currents were produced with D somewhat proportional to E. The energy dependence is possibly the result of crude focusing effects on the concave plasma sheath in the anode face. Figure 11 illustrates the offset effect; all parameters were held constant with the exception of focusing potentials.

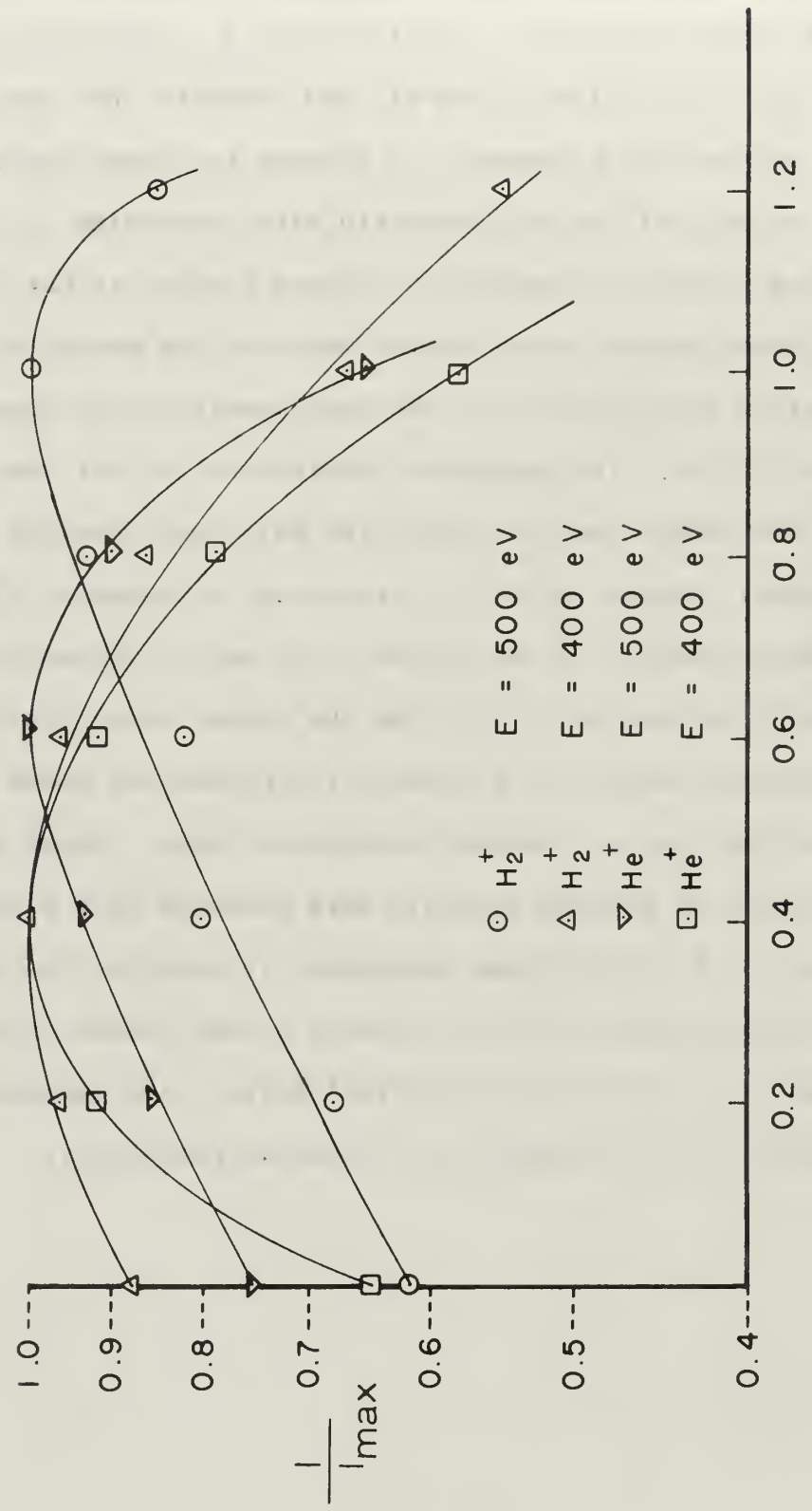


FIG. 11. RELATIVE BEAM CURRENT VS. Z. E. OFFSET.

Arc Current

The arc current operating range is 0.2 - 1.1 amps. This parameter accounts principally for electron density within the plasma, and hence for the plasma density. It is to a small degree responsible for ion beam intensity. Data has shown that the beam current varies by a factor of less than three over the entire arc current operating range, all other parameters save focusing held constant. At beam energies above 350 eV the effect is least noticeable; at lower accelerating potentials there appears to be a definite arc current strength at which beam intensity peaks. The location of the maximum has proved to be pressure dependent, though the relationship is not smooth. These findings are pictured in Fig. 12, which is a composite of two curves.

Since the primary factors in determining plasma density are electron current density, gas pressure, and ionization efficiency, the arc current dependence of ion beam intensity is an expected result. The relationship between the primary variables is more complicated. Clearly there is considerable choice in setting the involved parameters to obtain any desired beam intensity; secondary adjustment of several or all of the variables may be necessary to obtain optimum performance.

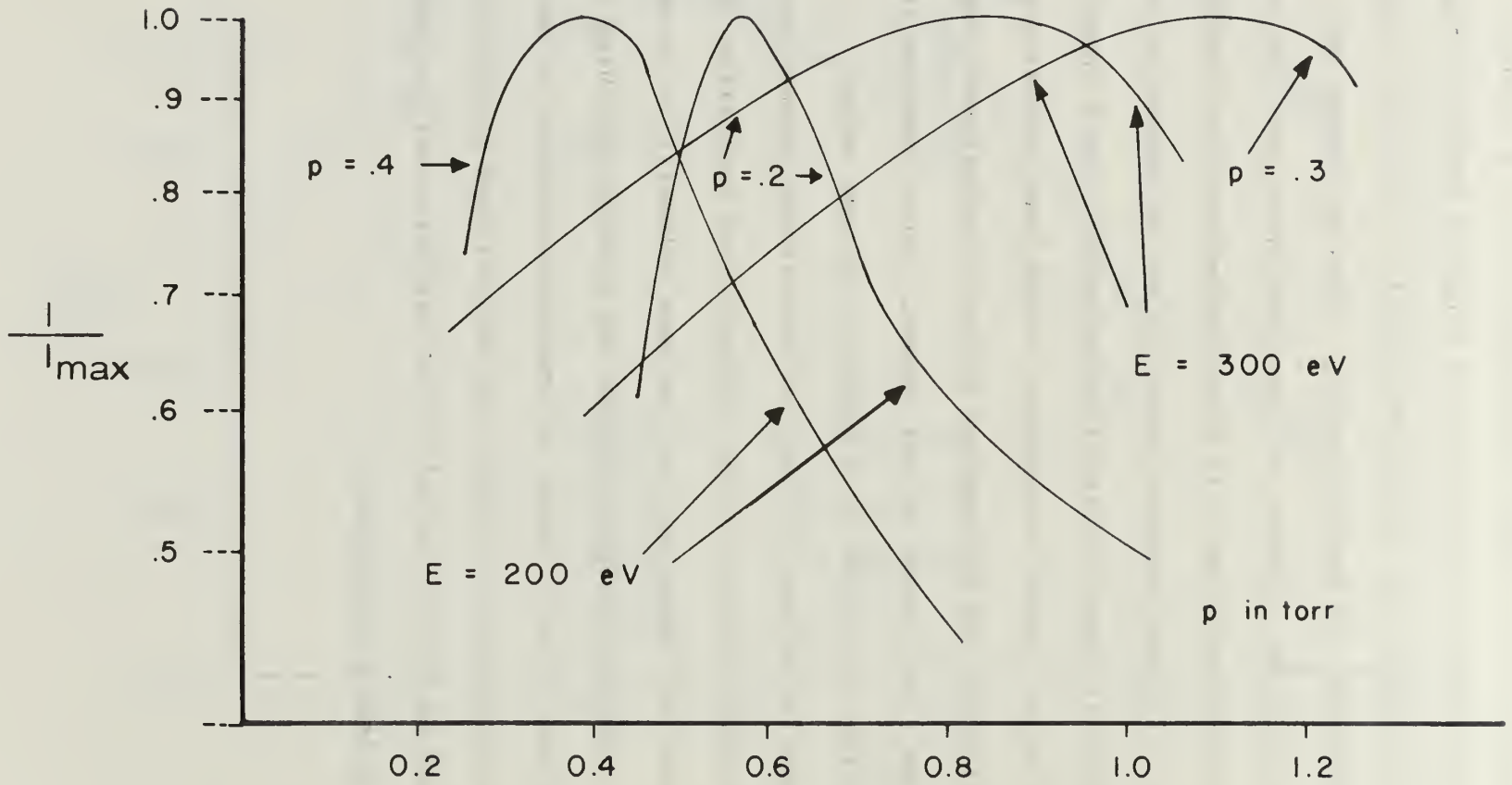


FIG. 12. RELATIVE BEAM CURRENT VS. ARC CURRENT

Source Gas Pressure

The dependence of beam current upon source gas pressure is more marked than the relationship between the ion beam and arc currents. Figure 13 illustrates the appearance of a sharp maximum in the ion beam intensity as pressure is varied, corresponding to the conduct predicted by Townsend discharge theory (equations A.13, A.14). The currents depicted were measured on a detector 7.6 cm in diameter, 55 cm from the duoplasmatron. The behavior takes place, briefly, because at pressures below $\hat{P}$, the mean free paths of electrons in the plasma are large and few can collide with gas molecules before impinging on the anode. At $P > \hat{P}$, the mean free paths become increasingly smaller and the number of electron-gas collisions rises. Few electrons, however, can acquire sufficient energy between collisions to produce ionizations. The peak value of beam current is closely related to the optimum value of s_e, ionization efficiency.

According to equation (A.14), $\hat{P}$ is directly proportional to the arc potential. It is imperative that atomic scattering experiments be carried out under low pressure conditions, and in this sense operating values of arc potential (arc current) should be minimized. In this manner $\hat{P}$ can be reduced. Ionization efficiency is also related to arc voltage (through electron energy), and it follows that the arc potential should be maintained at a particular, pressure related value to optimize the ionization process. This goes to illustrate what was mentioned in the previous section; numerous independent and interdependent parameters control ion beam intensity, and all must be continuously monitored to maximize the beam.

Discharges have been sustained at source pressures as low as 0.04 torr and as high as 0.7 torr, and the behavior of the ion beam current is always similar to that pictured in Fig. 13.

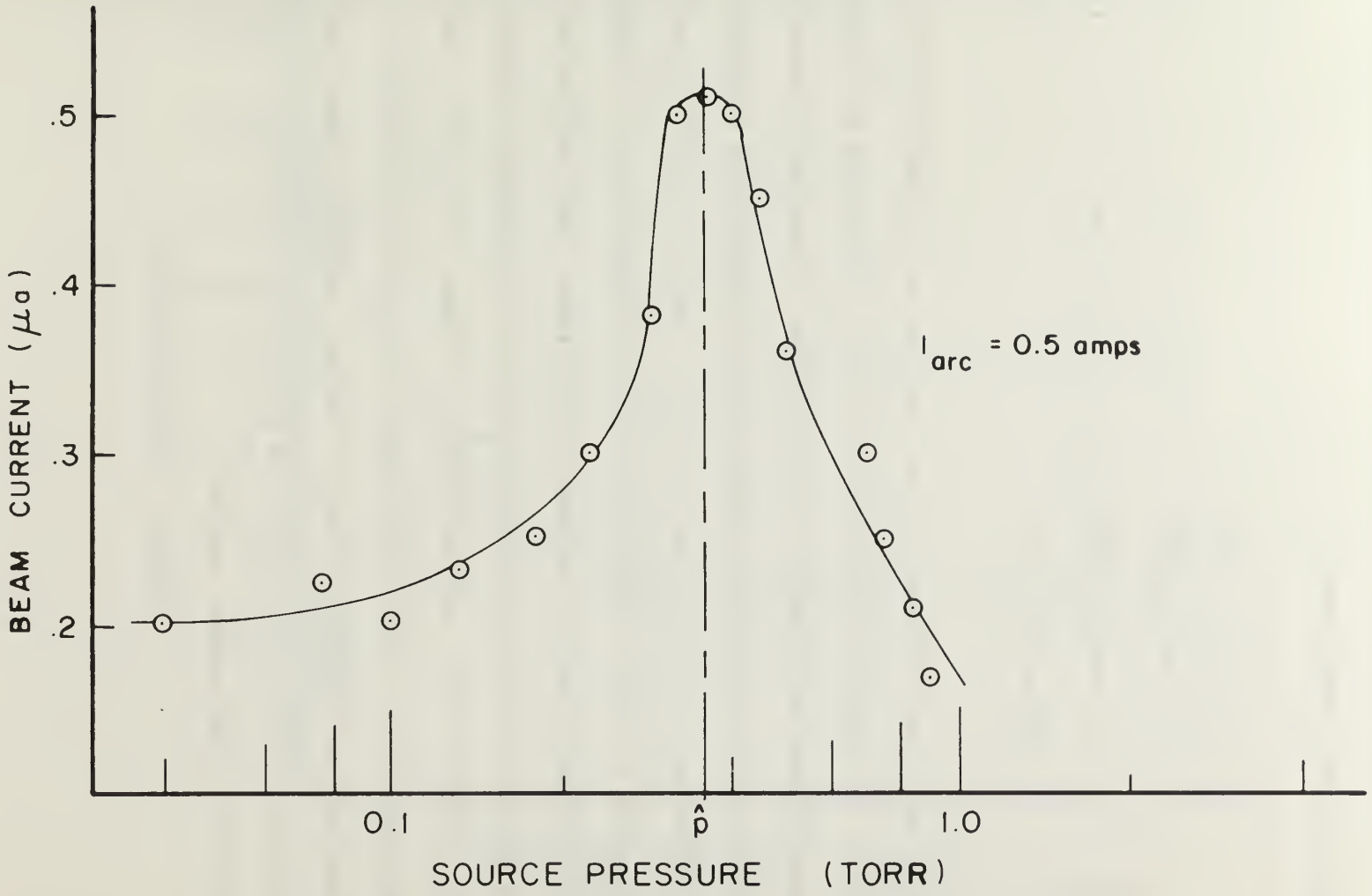


FIG. 13. BEAM CURRENT VS. SOURCE PRESSURE.

Mass Analysis and Magnetic Field Effects

The most important processes by which hydrogen ions are produced can be summarized as

$$H_2 + e \longrightarrow H_2^+ (^2\Sigma_g) + 2e \qquad \text{(III.2)}$$

$$H_2 + e \longrightarrow H_2^+ (^2\Sigma_u) + 2e \longrightarrow H + H^+ + 2e \qquad \text{(III.3)}$$

$$H_2 + e \longrightarrow H_2^+ (^2\Sigma_g) + 2e \longrightarrow H + H^+ + 2e \qquad \text{(III.4)}$$

$$H_2 + H_2^+ \longrightarrow H_3^+ + H \qquad \text{(III.5)}$$

where the total ionization cross section for process (III.3) and (III.4) is roughly 0.005 that of (III.2). Actually the observed concentration of H^+ ions is much greater, therefore protons must be produced in increased numbers involving multiple processes such as indicated in (III.3) and (III.4). The ratio of H^+/H_2^+ can be increased if losses within the arc and recombination of molecular ions and electrons are broughtto a minimum. The application of the magnetic field on the plasma serves this purpose (Section VIII, Chapter III), and the effect is shown in Fig. 14. Data was taken using a mass spectrometer, varying only focusing potentials and magnet current. The mass analysis shows that H^+ production never exceeds that of H_2^+, and is maximized in the region of a 1 amp magnet current.

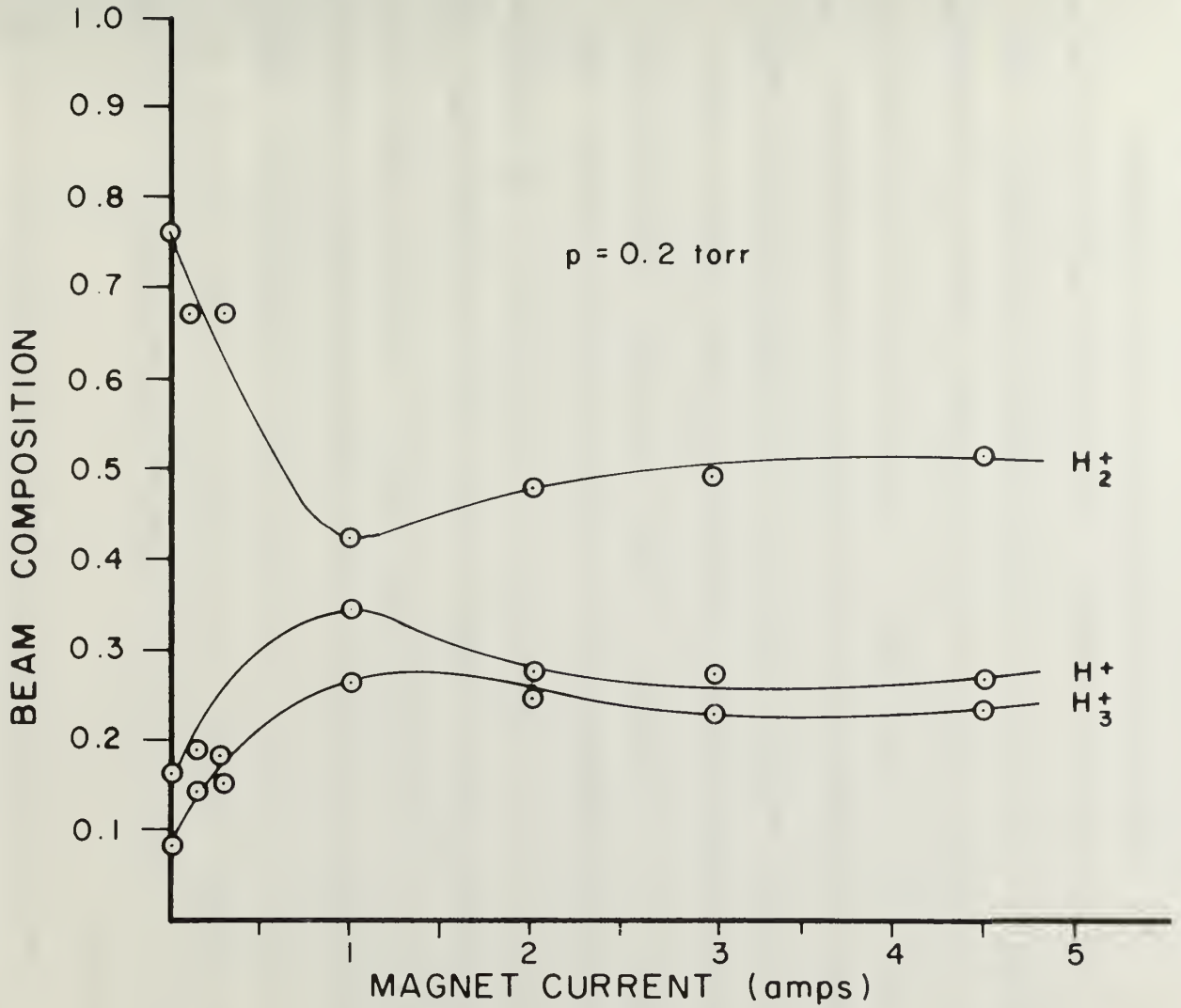


FIG. 14. BEAM COMPOSITION VS. MAGNET CURRENT.

Energy Analysis

An electrostatic energy analyzer was used to measure the energy dispersion and beam energy of the total hydrogen beam. Measurements on each hydrogen species were not performed, but the results for the total beam should apply to each component.

Energy spread measurements were made in a manner described by Strohsahl[1]. For each of the beam energies investigated, a curve similar to that in Fig. 15 was constructed, from which ΔE was taken. A summary of the measurements is found in Fig. 16. The results are somewhat disappointing in that an ideal beam is monoenergetic, but good evidence indicates that much of the energy dispersion found using our method is due to analyzer resolution effects. In Appendix D it is pointed out that the analyzer shows ΔE for an essentially monoenergetic Li^+ ion beam to vary up to 5 eV. The resolution of the energy analyzer is proportional to the potential applied to the device, which is some fraction of beam energy. This results in an undesirably broad analyzer transmission function at high accelerating potentials, and the measured energy spread can be far greater than that of the actual beam (see Appendix D). Accel-decel methods could be used to retard an ion beam just prior to analysis in order to operate the measuring instrument at very low potentials.

A very plausible source of some energy dispersion in the ion beam is that acquired by ions of the plasma passing through the anode fall region of the duoplasmatron extraction stage (Section VIII, Chapter III), due to asymmetry of the space charge sheath and magnetic field surrounding the anode aperture (Fig. 9). This energy

spread could amount to from 2-3 eV up to about 10 eV, depending upon the exact location of the ions in the Z.E. -anode gap from which they are extracted to the anode face. Based on (i) the magnifying effect of the analyzer as shown for lithium ion beams, (ii) the $\sim$ 3.5 eV energy spread of the duoplasmatron hydrogen ion beam at E = 100 eV (Fig. 16), and (iii) the fact that there is no evidence that this source of energy dispersion is dependent upon extraction potentials, we would expect the average energy spread due to this cause to be nearly constant and of magnitude less than 3 eV.

The beam energy is essentially determined by the plasma potential, which is equal to the potential of the anode plus the anode fall (4-10 volts). However, as positive ions are extracted from the plasma in the anode face, an equivalent electron current (0.05-0.8 ma) drifts back into the anode. This virtual battery lowers the anode potential by $\sim$ 1-18 volts from that set on the accelerating power supply. The resultant plasma potential is therefore lower than that indicated by up to $\sim$ 14 volts. The behavior of this discrepancy is regular, and a beam energy calibration curve has been constructed (Fig. 17).

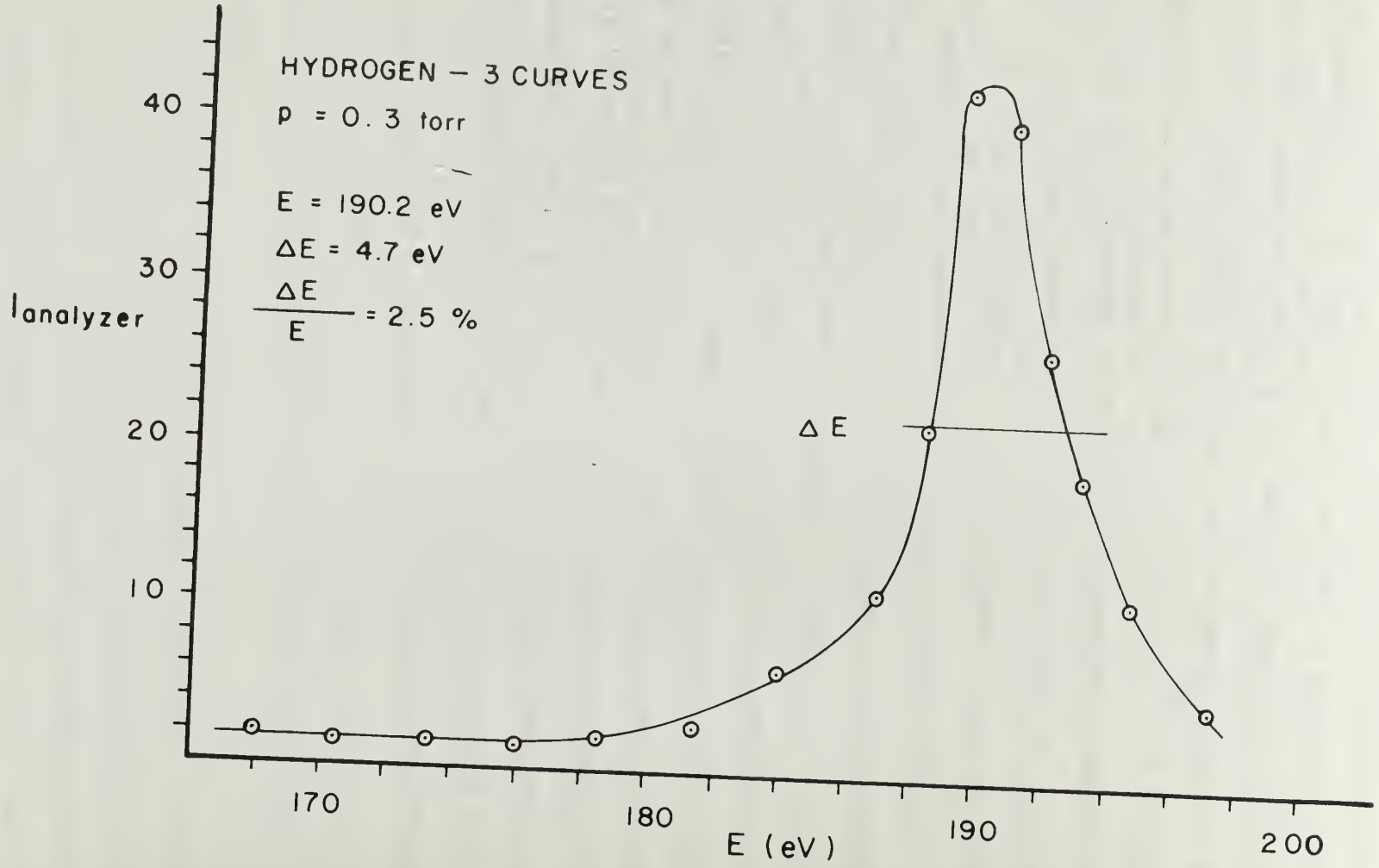


FIG. 15. ENERGY ANALYZER CURRENT VS. BEAM ENERGY

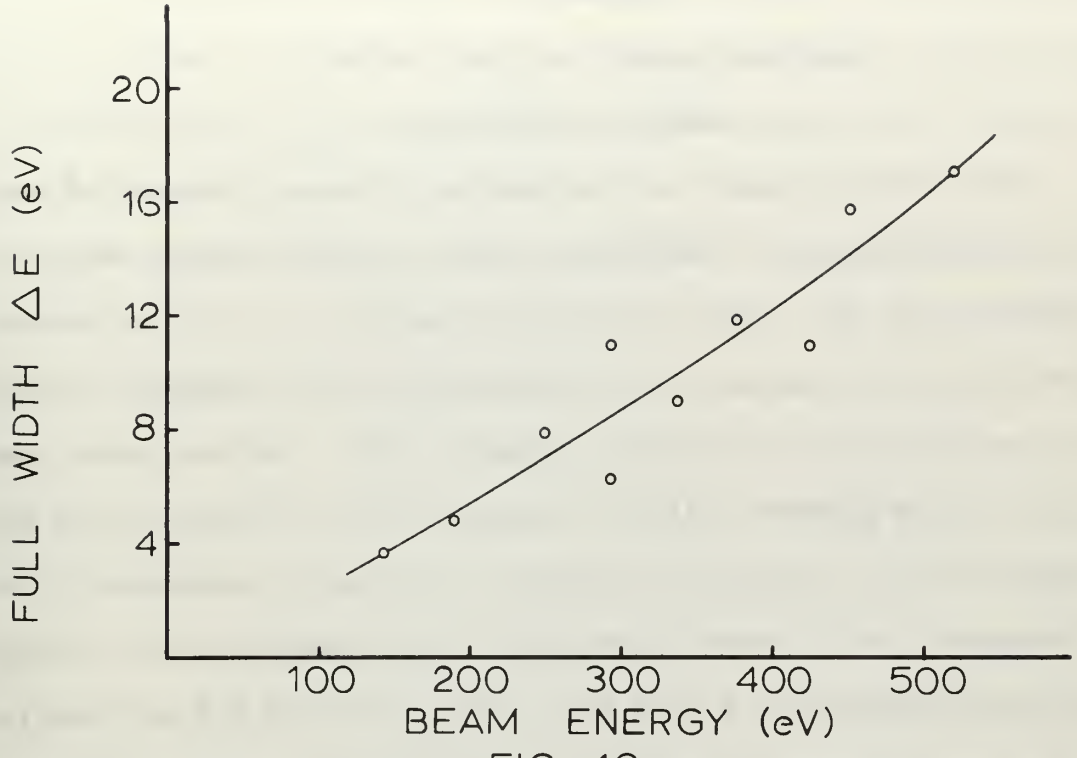


FIG. 16.

ENERGY DISPERSION vs. BEAM ENERGY

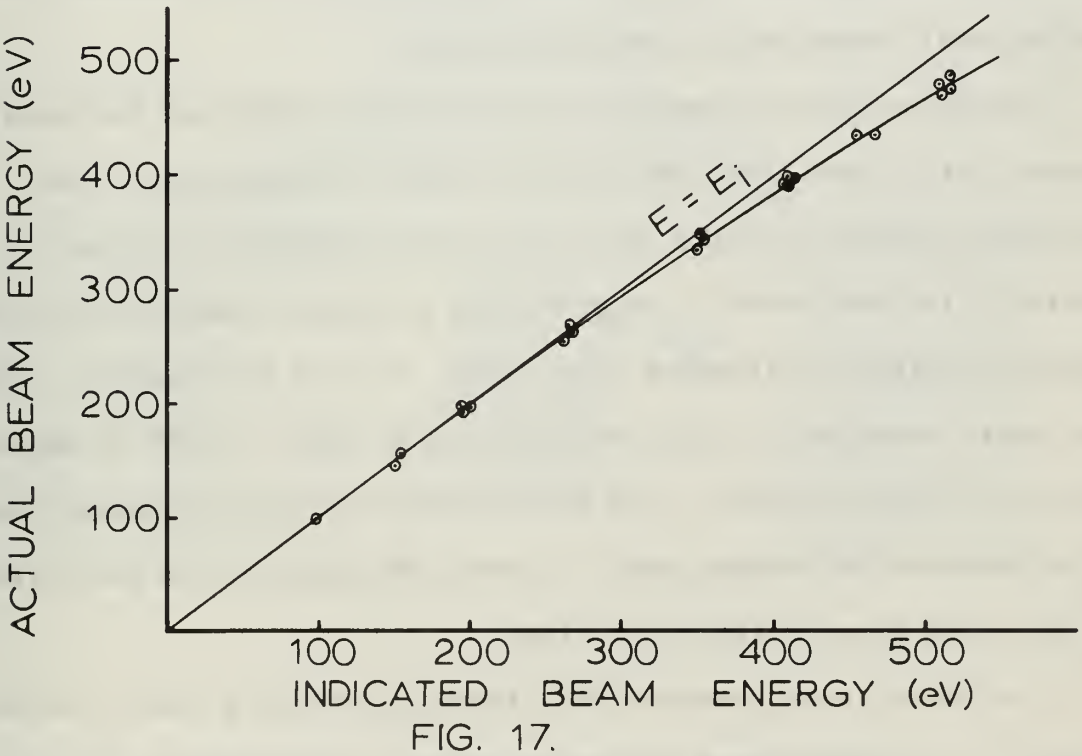


FIG. 17.

BEAM ENERGY CALIBRATION CURVE.

CHAPTER IV

ELECTRON IMPACT GAS ION SOURCE

I. SOURCE CONSTRUCTION

The electron impact gas ion source is shown in Figs. 18 and 19. It consists of a discharge chamber and focus stack, with accomodation for gas entry and pressure control. A 5.7 cm diameter glass press base supports the filament and grid, mounted concentrically on four 1.59 mm diameter tungsten rods. The two inner rods hold a 1.3 cm diameter helical filament made of 15 mil (0.375 mm) tungsten wire. The grid is similarly configured, measures 2.5 cm in diameter, and is held by the outer two tungsten rods. Both the grid and filament are 3.8 cm high, and positioned 3.8 cm from the base of the inverted glass press. It was found necessary to recess the tungsten support rods in the well of the press to prevent shorting my metal evaporating from the filament.

The glass press assembly is electrically insulated and mounted inside a stainless steel can of 5.7 x 13.1 cm dimensions. The extraction aperture of the can is 0.5 cm in diameter, axially located. The electrode is supported by a lavite ring which provides insulation from the aluminum base plate, 21.5 cm in diameter. The base plate contains a 0.635 cm ID gas inlet pipe, a 0.95 cm Bayard-Alpert ion gauge fitting, nine kovar electrical feed-throughs, and an O-ring seat for vacuum seal. A Hoke 280 series metering valve in the inlet pipe controls gas flow.

The focus stack consists of a three-electrode einzel lens and two pairs of opposed beam deflector shims. Each lens is separated

by 1.4 cm and has an axially aligned 1.4 cm bore. On one of the three sources on hand the deflector shims have been replaced with a grounded extraction grid, located between the einzel lens and the extraction aperture of the can.

The wiring diagram for the ion source is shown in Fig. 20.

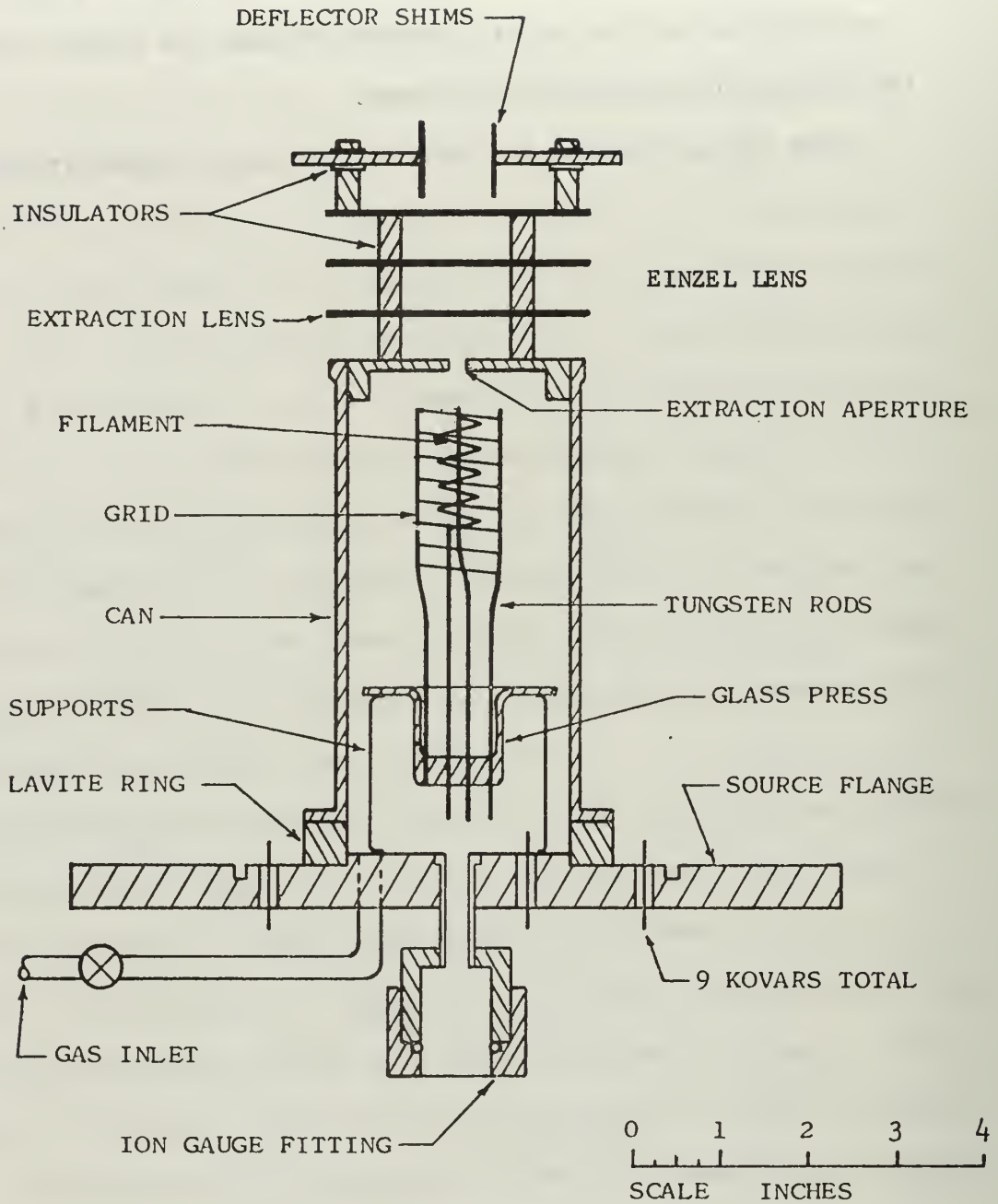


FIG. 18.

ELECTRON-IMPACT GAS ION SOURCE

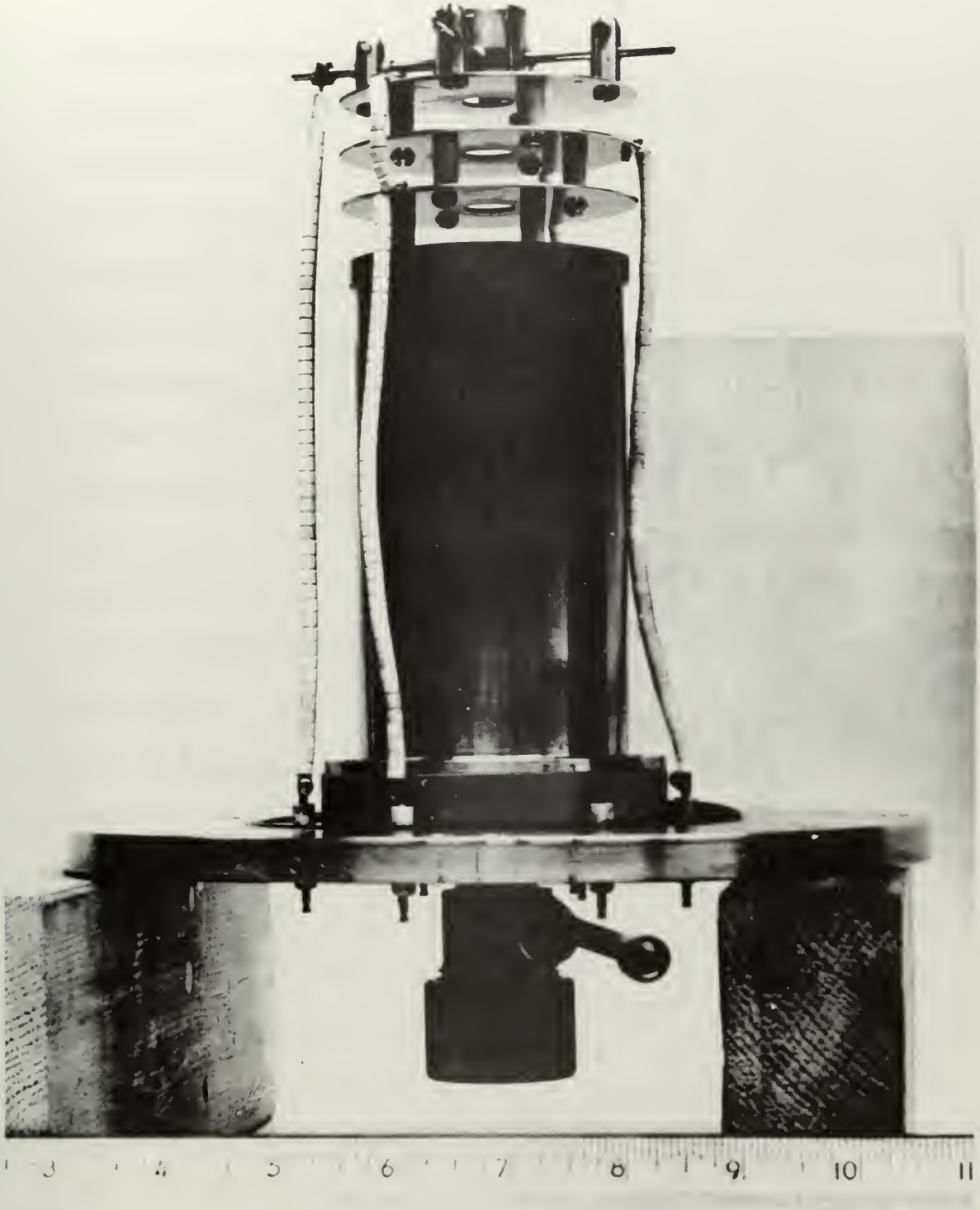


FIG. 19.
EXTERNAL VIEW OF ION SOURCE

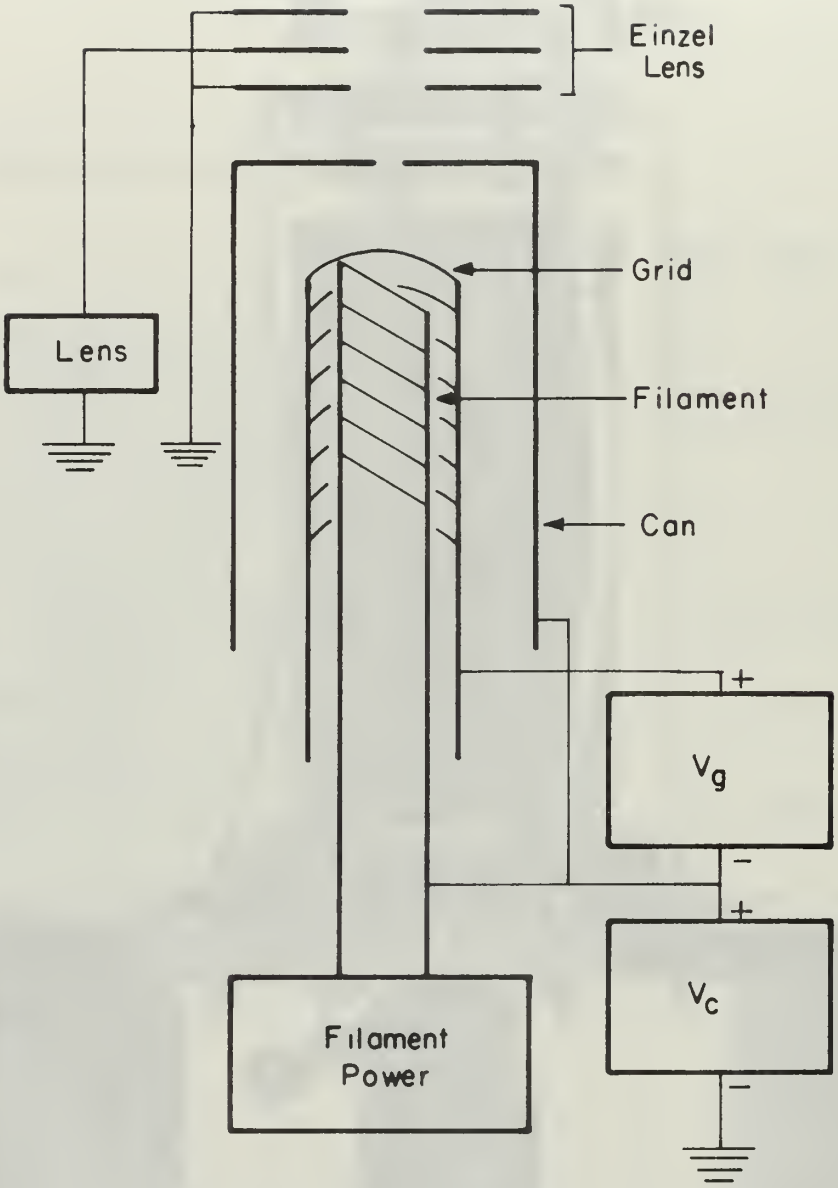


FIG. 20.

CIRCUITRY SCHEMATIC FOR
ELECTRON-IMPACT ION SOURCE.

II. OPERATING CHARACTERISTICS

Ions are produced in the source by electron impact with gas atoms. Behavior of the source indicated that a Townsend discharge in the T_1 region takes place, and grid current and voltage appear much like that pictured in Fig. 34. Sustained operation is made possible by the electron emission of the hot cathode. The grid is floated at a potential above the common filament-can potential, and provides the necessary electric field for the gas discharge. With a gas pressure in the region of 10^{-3} torr in the can, electrons are thermally generated from the filament and accelerated toward the grid. Those which do not impinge on the grid are reversed in direction by the grid-to-can electric field. In this manner electrons are caused to oscillate around the grid: the number of ion pairs produced is a function of the time they spend in motion. Both gas pressure and grid voltage are adjusted to the operating values to raise the grid current to 75 ma, the plateau region of the Townsend discharge. Typical grid current/grid voltage behavior is shown in Fig. 21. Typical grid current/source pressure behavior appears in Fig. 22. The arc discharge region is clearly seen in each case.

The operating filament power is ~ 200 watts, which corresponds to 1900°C and a filament current of 11 amps. It was discovered that filament currents above 12 amps cause a marked increase in grid current at operating pressures due to high filament electron emission. Filament currents smaller than 10 amps yield insufficient electron emission to initiate the discharge. In time, filament aging changes the power requirements for emission. Both DC and AC power supplies

have been used, and power consumption has varied between 150-250 watts. This is a slowly changing parameter, of little importance in day-to-day operation.

The pressure dependence of the ion beam intensity is seen in Figs. 23-25. For the two gases tested, hydrogen and nitrogen, general characteristics were the same. Low beam currents are produced at pressures of less than 10^{-3} torr; a sharp increase is observed at or near that pressure; a maximum is reached at about 3×10^{-3} torr; and a gradual decrease in beam current follows as pressure is further increased. The steep rise in I_{beam} denotes arc discharge initiation, and takes place at a critical pressure, P_i. The rate of decrease of beam intensity at pressures higher than P_i is greater for heavier species than for light ones. The maximum observed is simply that predicted by Townsend discharge theory (equation A.14).

Closely related to pressure dependence of beam current is the pressure effect on beam energy. A plasma normally assumes a potential near that of the most positive element in its surroundings, and a beam energy equal to the sum of the can and grid voltages is the observed condition at source pressures greater than P_i. Data shows, however, that at pressures below P_i the beam energy is less by an amount equal to V_g. It is clear that before the arc discharge takes place we do not have a plasma potential and the ions which are produced have the energy of the can voltage only. For this reason, pressure control is paramount in the source operation.

Breakdown potentials for three gases investigated with this source were determined to be: H_2, 80 volts; He, 90 volts; and N_2, 36 volts, at a pressure of 3×10^{-3} torr. Increase of V_g above the breakdown voltage causes only a slight decrease in the beam current, and V_g = 100 v has been confirmed for general use. The behavior of beam intensity with grid current is shown in Fig. 26. The hysteresis seen is due to prolonged discharge caused by residual electrons oscillating around the grid. Sustained operation in the hysteresis region is impossible due to eventual loss of the electron flux, hence arc discharge.

Figures 24 and 25 demonstrate that for a given gas, production of certain species is favored over others, and that the dependence is pressure related. With hydrogen in the source, the probable set of reactions are given by equations (III.2) through (III.5). The predominance of H_2^+ over H^+ in the source follows for the same reasons as in the case of the duoplasmatron. The dominance of H_3^+ ions over H_2^+ at $P > 3 \times 10^{-3}$ torr is probably due to a change in one of the collision parameters, namely electron energy, brought about plasma density and space charge effects within the arc discharge.

The probable set of processes for the production of N_2^+ and N^+ is

$$N_2 + e \longrightarrow N_2^+ + 2e \qquad \text{(IV.1)}$$

$$N_2 + e \longrightarrow N^+ + N + 2e \qquad \text{(IV.2)}$$

$$N_2^+ + e \longrightarrow N^+ + N + e \qquad \text{(IV.3)}$$

$$N + e \longrightarrow N^+ + 2e \qquad \text{(IV.4)}$$

The emergence of N^+ ions as the more numerous species at $p > 4 \times 10^{-3}$ torr indicates that the probability for process (IV.2) becomes greater than that for process (IV.1) at that pressure.

An attempt was made to increase the H^+ output of this source by the addition of water vapor in the discharge region. The water vapor was let into the source from an evacuated beaker charged with ice. Mass analysis of the resultant ion beam was made at three different source pressures, and the production of H^+ increased with an increasing ratio of water to hydrogen gas. The vacuum pumping problems associated with this technique, however, rule it impractical.

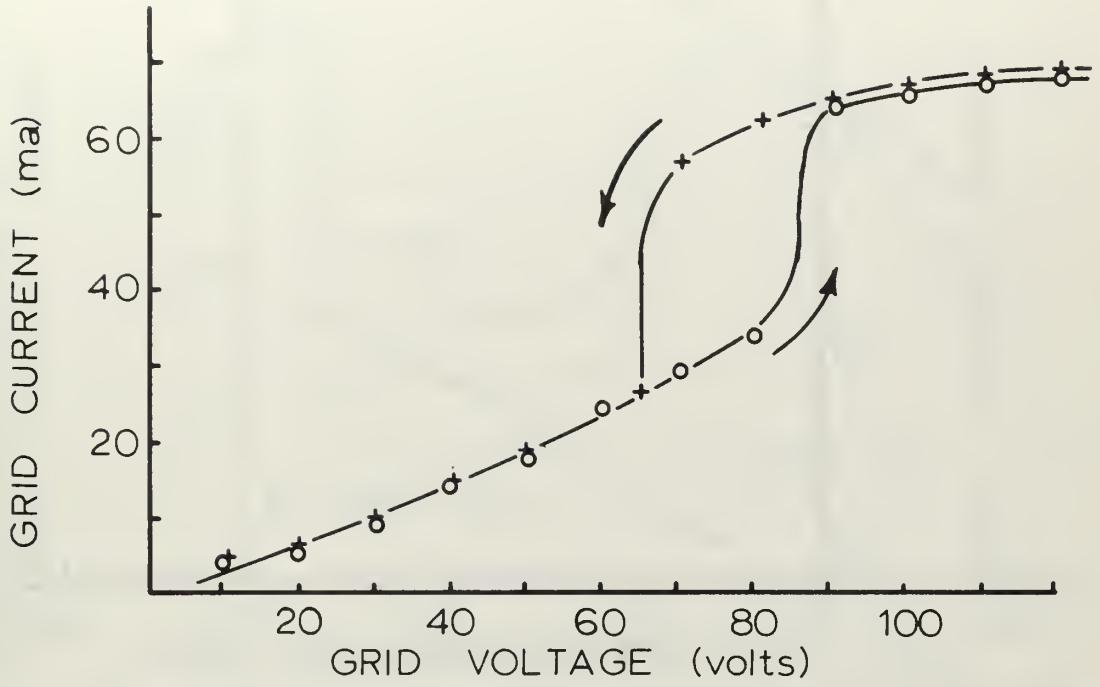


FIG. 21.

GRID CURRENT vs. GRID VOLTAGE

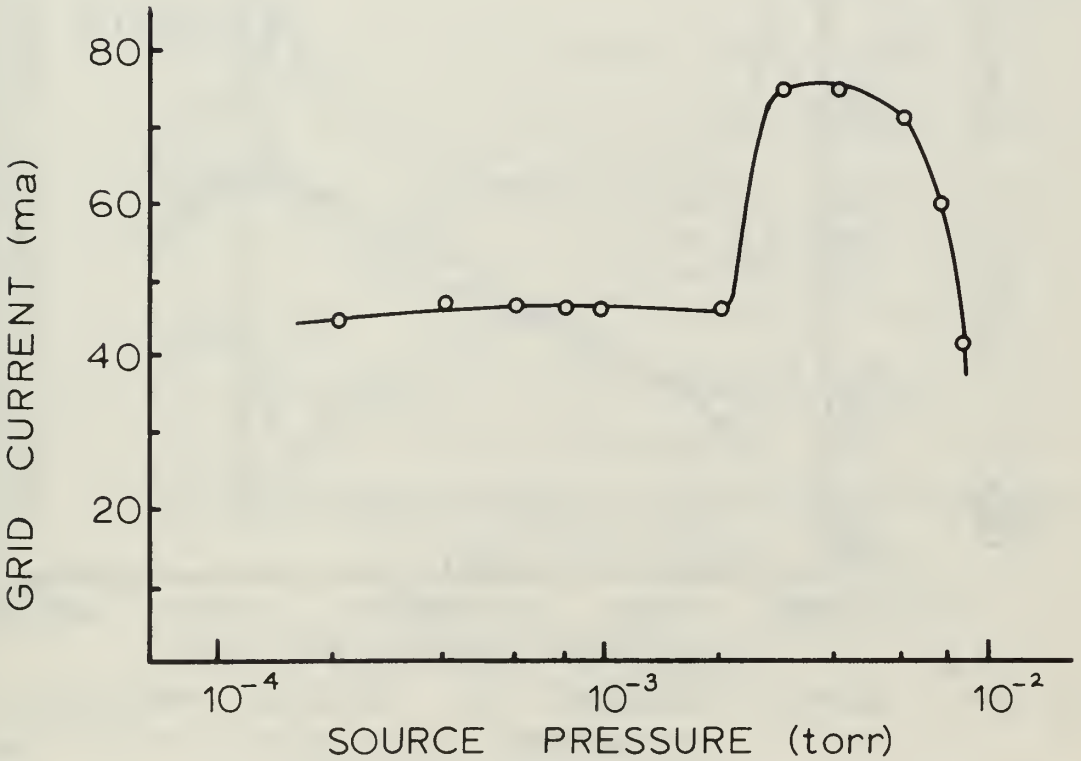


FIG. 22. GRID CURRENT vs. SOURCE PRESSURE

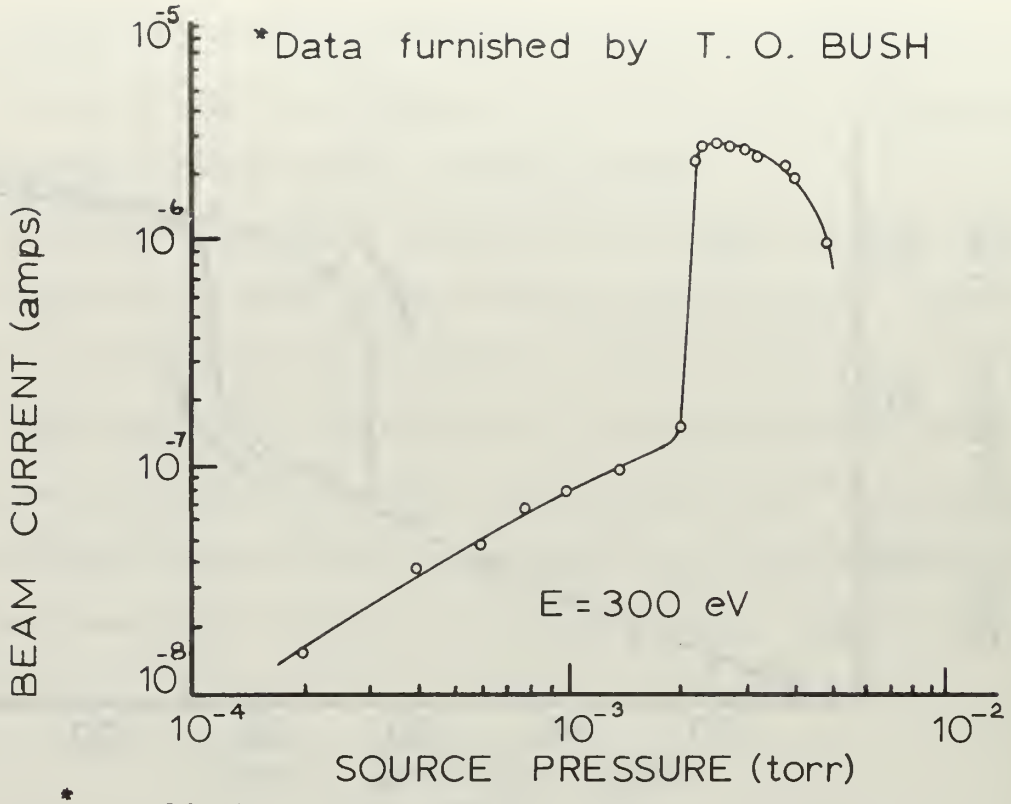


FIG. 23.* TOTAL HYDROGEN BEAM INTENSITY vs. SOURCE PRESSURE

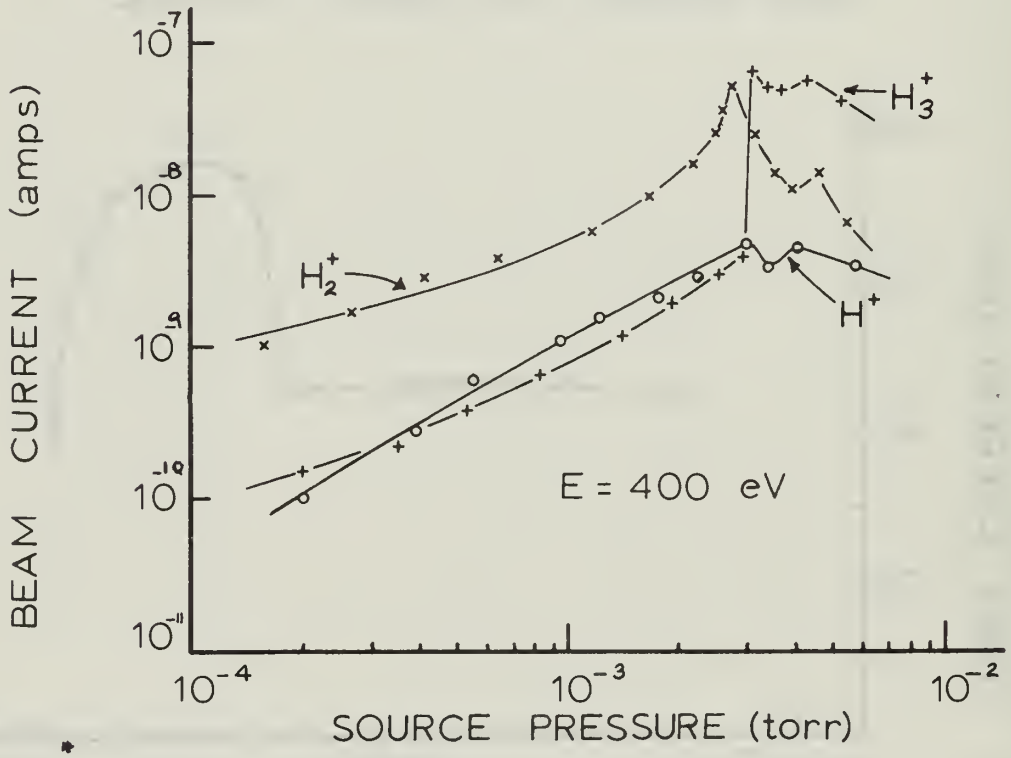


FIG. 24.* BEAM CURRENT vs. SOURCE PRESSURE, HYDROGEN SPECIES

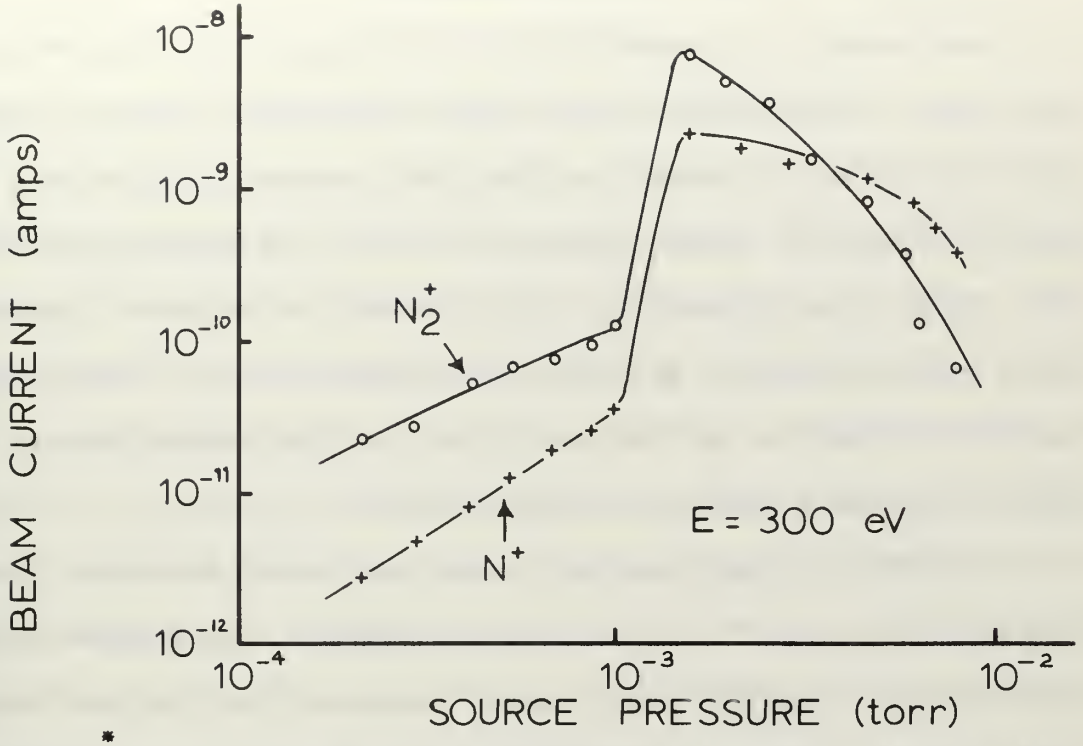


FIG. 25.* NITROGEN ION CURRENT v. SOURCE PRESSURE

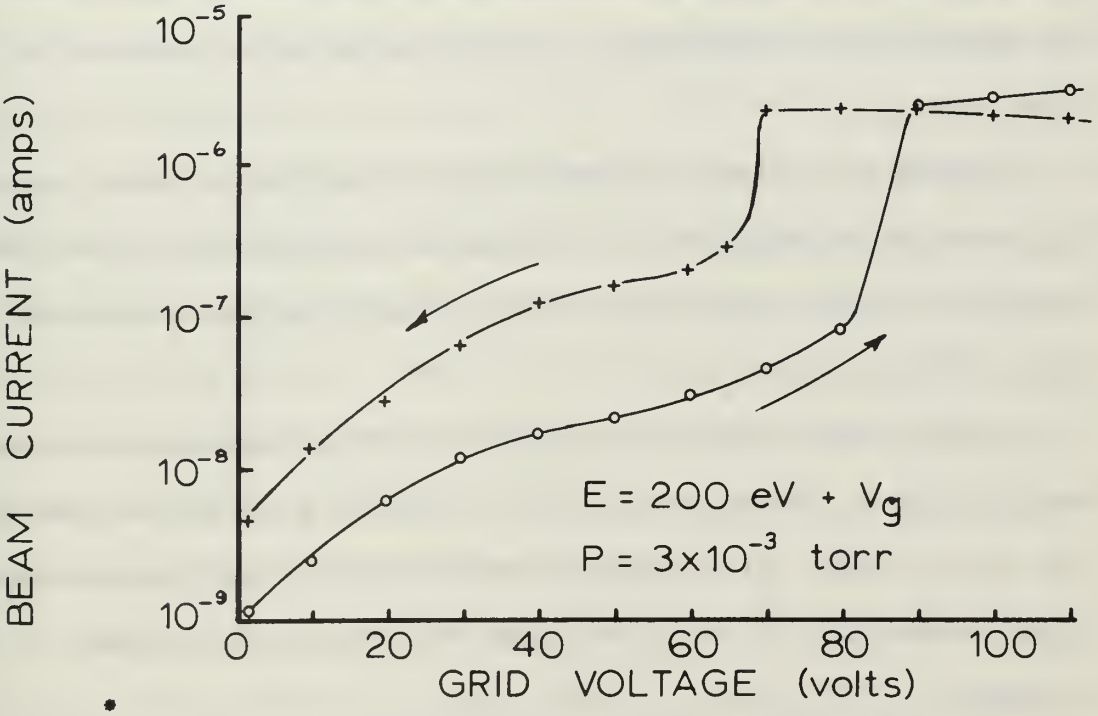


FIG. 26.* TOTAL HYDROGEN BEAM INTENSITY vs. GRID VOLTAGE

*Data furnished by T. O. Bush

III. SOURCE OPERATION

The source is operated by first setting the grid potential at 100 volts. Care must be taken in the choice of a DC power supply for this, so as to insure that spurious currents of up to 0.4 amps can be withstood. As has been pointed out, the operating current is ~ 75 ma. The filament is brought slowly to emission temperature, which will establish a grid current of about 50 ma. The can potential is then set so that this plus the grid voltage equals the desired ion beam energy in electron volts.

As with the duoplasmatron, gases are passed through a liquid nitrogen trap prior to entry into the source. Gas is bled into the source until breakdown takes place, at which time the grid current rises rapidly. Once the discharge is established, minor pressure and grid voltage adjustments can be made in order to maximize the beam current.

Arcing has occurred between the can and focus stack at source can voltages of about 500 v, setting an upper limit on the beam energy available. The lower limit is the breakdown potential particular to each gas, V_s.

Beam intensities in the range of 10 microamps were obtained from both H_2 and N_2, as measured with a collecting plate just ahead of the focus stack. At a current detector 75 cm downstream maximum beam intensities of ~ 0.2 microamps/cm^2 have been achieved at 400 eV energy.

CHAPTER V

LITHIUM ION SOURCE

I. ION EMITTER AND SOURCE CONSTRUCTION

The lithium ion emitter (Fig. 27) was first reported on by Haskell, Heinz, and Lorents[4] in 1965. Improvements have been made since then, and the emitter is now commercially available. The emitting surface is a specially prepared extremely porous tungsten disc (30% matrix density) heliarc welded to a molybdenum body. The plug is impregnated with mineral β-eucryptite ($Li_2O \cdot Al_2O_3 \cdot 2\ SiO_2$) to a depth of about 0.5 cm by placing controlled amounts of the face and melting at ~ 1650°C in a hydrogen atmosphere. Beams of either $^6Li^+$ or $^7Li^+$ can be produced by using isotopically enriched $LiCO_3$ in the preparation of the β-eucryptite.

The active lithium emitter is isolated from the heater cavity by an integral web in the moly body. The heater is a non-inductively wound tungsten wire with heliarc welded rhenium leads solidly potted into the body cavity. The high purity Al_2O_3 potting mix is hydrogen fired at 1900°C which completely immoblilizes and electrically insulates the heater. Attached to the moly body at 120° separation are three ruthenium and nickel alloy support struts brazed on with a moly/ruthenium utectic at 2100°C in hydrogen. A moly foil heat shield is attached around the assembly.

The emitter is mounted to a stainless steel support ring by means of the ruthenium struts, which is then fixed atop stainless steel legs anchored in an 21.5 cm diameter aluminum flange, forming the source proper. The flange contains the necessary kovar electrical feed-throughs. The source is shown in Figs. 28 and 29.

The beam extraction stage is a standard three-element, plane-electrode einzel lens, with a single grounded extraction grid inserted next to the emitter. Separation between all elements of the focus stack is 1.4 cm, commencing with the extraction lens and emitting surface. The lens apertures are 1.4 cm in diameter.

II. OPERATING CHARACTERISTICS

Emission performance at beam energy 200 eV is shown in Fig. 30, which is a composite of two curves. Temperature measurements were made using an optical pyrometer looking directly into the face of the emitter. Total emission current was collected on a detector 6 cm in front of the emitter, using a suppressor grid and voltage of -22.5 v to suppress secondary electrons from the collector. The results of these measurements indicate that current densities of $\sim 20\ \mu a/cm^2$ can be obtained near the emitter at the extraction potentials used.

Emission temperature ranges from 900-1200°C, though emission becomes limited at temperatures greater than 1150°C. That temperature has been established as the operating value, and requires a filament power of ~ 90 watts. The maximum current which can be obtained from a plane diode emitter is given by the well-known Langmuir-Child equation ($I \sim E^{3/2}$). Emission at extraction energies below 200 eV behaves accordingly, but above that energy an emission limit is encountered and beam current levels off (Fig. 32). Using electrostatic focussing on a detector 35 cm downstream, measured beam intensities range from 10^{-10} amps at very low energies (a few eV) to 10^{-7} amps at around 500 eV, lower than the Langmuir-Child prediction by factors of 10-100. Although these currents are small, they are adequate for many atomic scattering experiments.

Mass analysis of a new emitter shows the beam composition to be 98% lithium, with Na_{23} and K_{39} impurities on the order of a percent each at operating temperatures. In β-eucryptite prepared from lithium enriched in Li_7, the amount of Li_6 observed is less than 0.01%, and vice versa. Figure 31 shows the behavior below 1100°C; the appearance of beam impurities increases to 10%, primarily Na and K, but also a trace of Rb_{85}. The impurities tend to be driven off after prolonged operation. A search for negative lithium ions showed that none were present.

Haskell, Heinz, and Lorents[4] made energy dispersion studies of the lithium beam at energies 22.76-4.53 eV. Analytical data showed ΔE, the full width energy spread at half maximum beam energy E, to be between 0.22 and 0.25 eV, and independent of beam energy in that range. This finding is supported by theory, in that the Maxwellian energy distribution of a thermal source at 1150°C is ~ 0.25 eV. Energy analyses at beam energies in the 35-500 eV range have been less conclusive. Since the energy resolution of an electrostatic analyzer is proportional to the mean beam energy its resolution becomes too broad for accurate measurements in this energy range.

III. SOURCE OPERATION

The ion gun is operated by first placing the emitter at a potential equal to the desired beam energy in eV, and grounding the extraction lens. Electrical shorting occurs in the heater cavity between the filament and emitter body at potential differences of ~ 400 volts, a problem circumvented by electrically floating the filament on the emitter power supply, as pictured in the insert, Fig. 30.

The filament is heated to operating temperature corresponding to about 90 watts power usage. Both AC and DC power supplies have been utilized. The einzel lens is operated in the normal manner, with a variable potential placed on the middle lens and the first and third lenses held at ground.

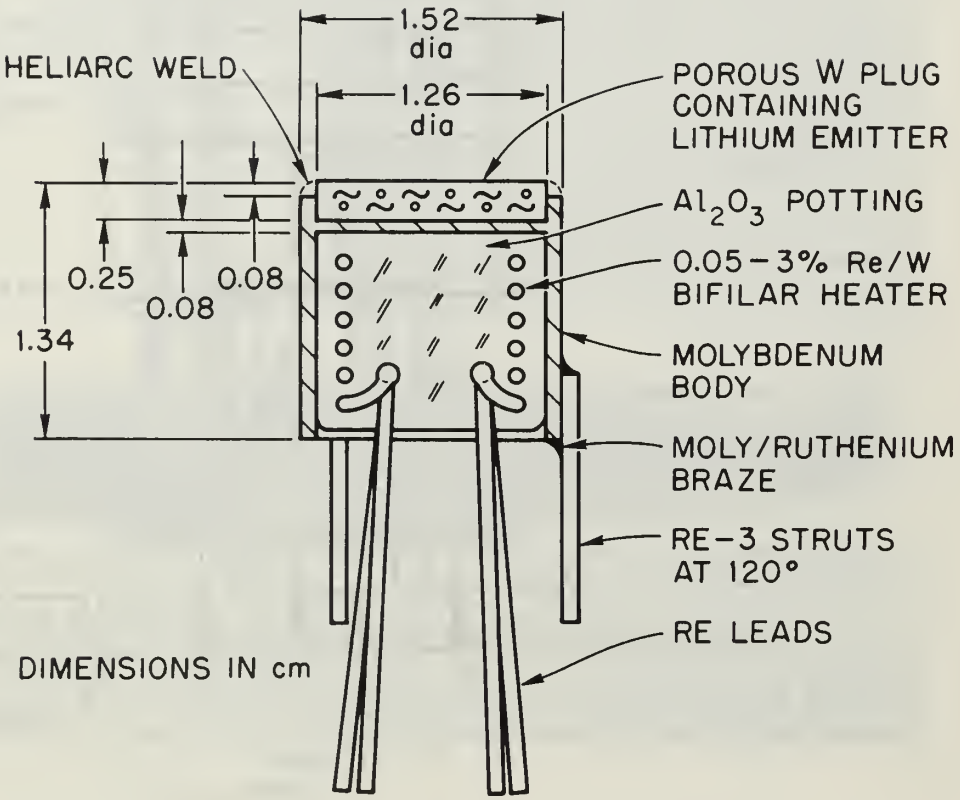


FIG. 27.

LITHIUM ION EMITTER

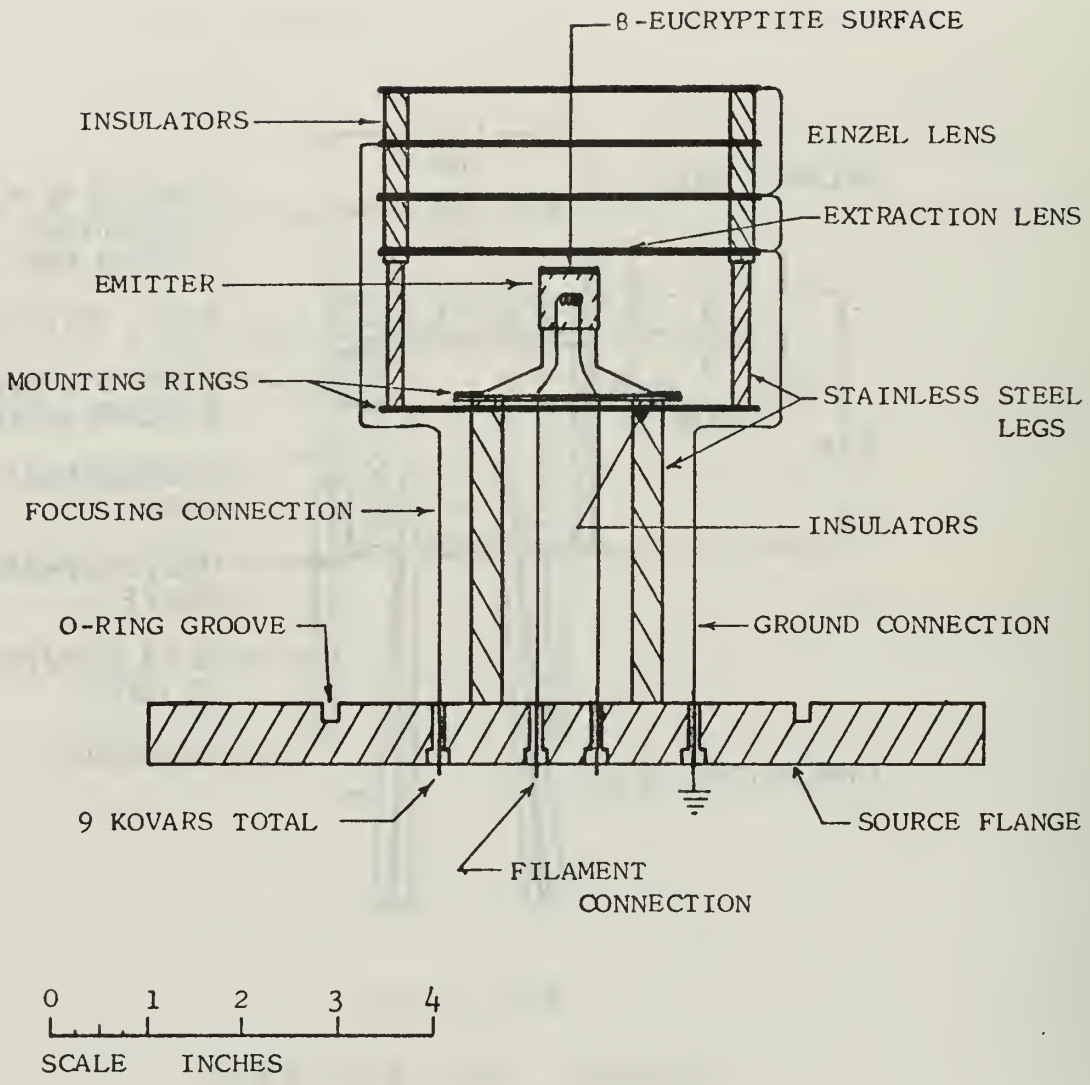


FIG. 28.

LITHIUM ION SOURCE

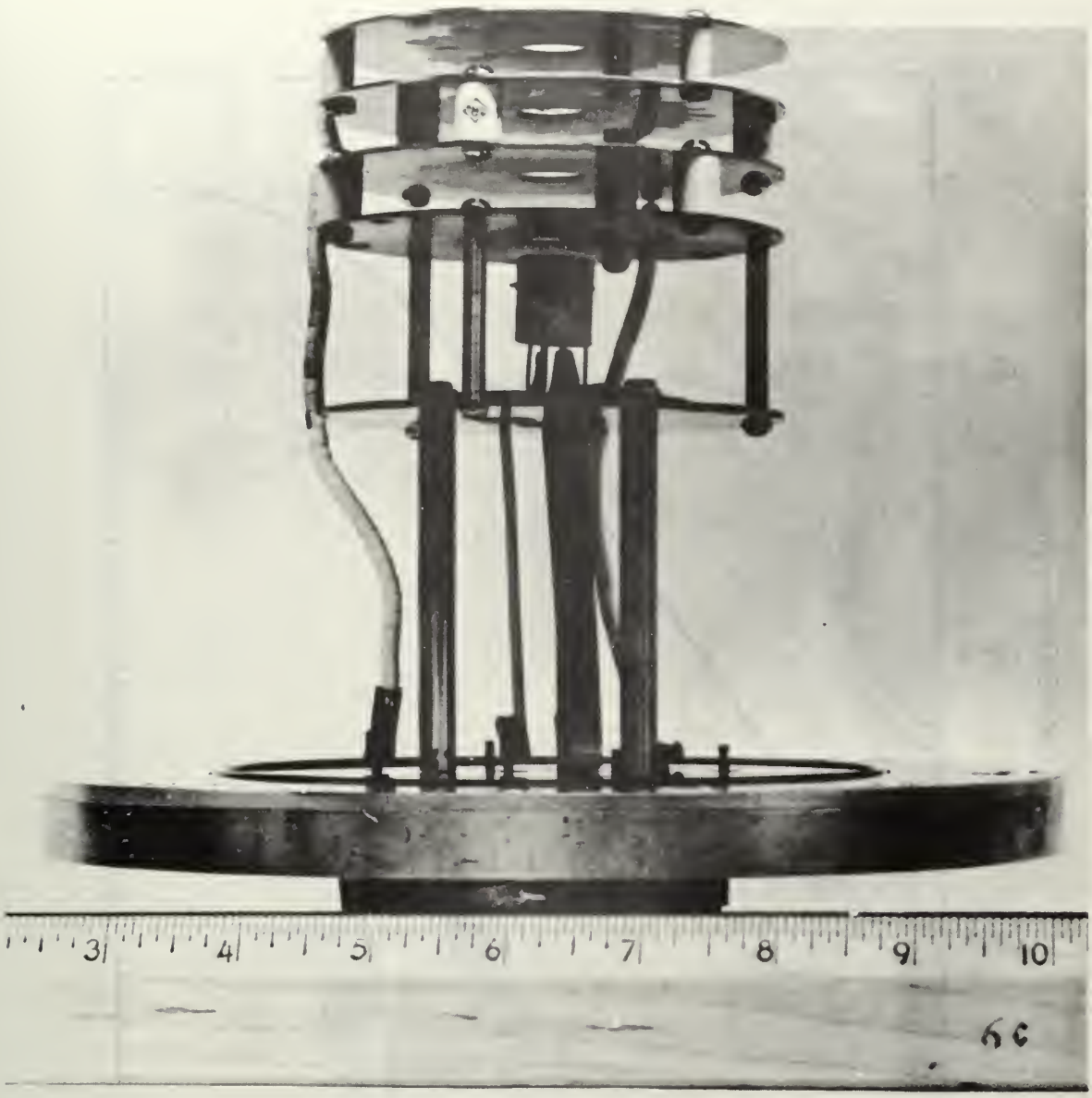


FIG. 29.

EXTERNAL VIEW OF LITHIUM ION SOURCE

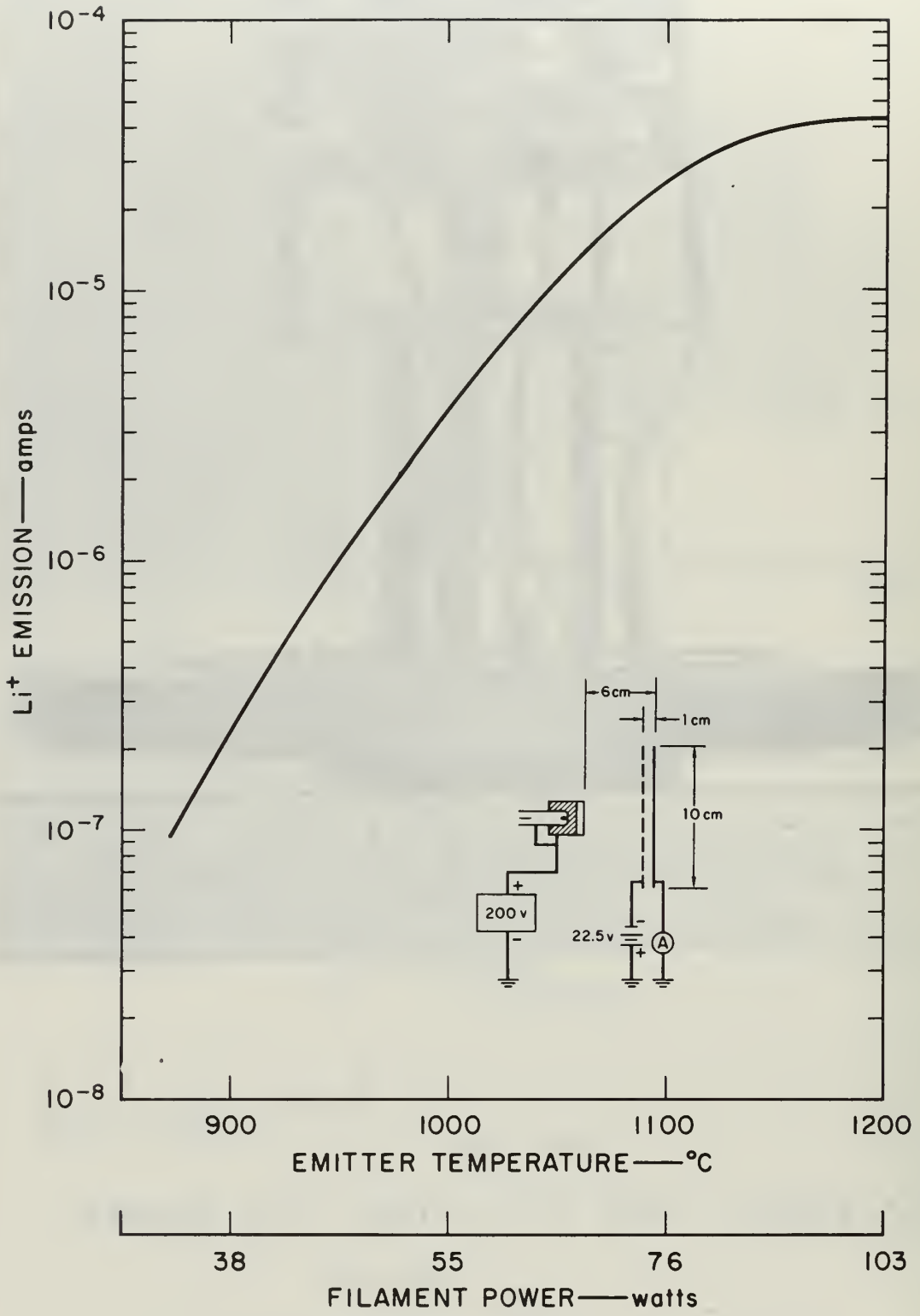


FIG. 30. LITHIUM SOURCE EMISSION

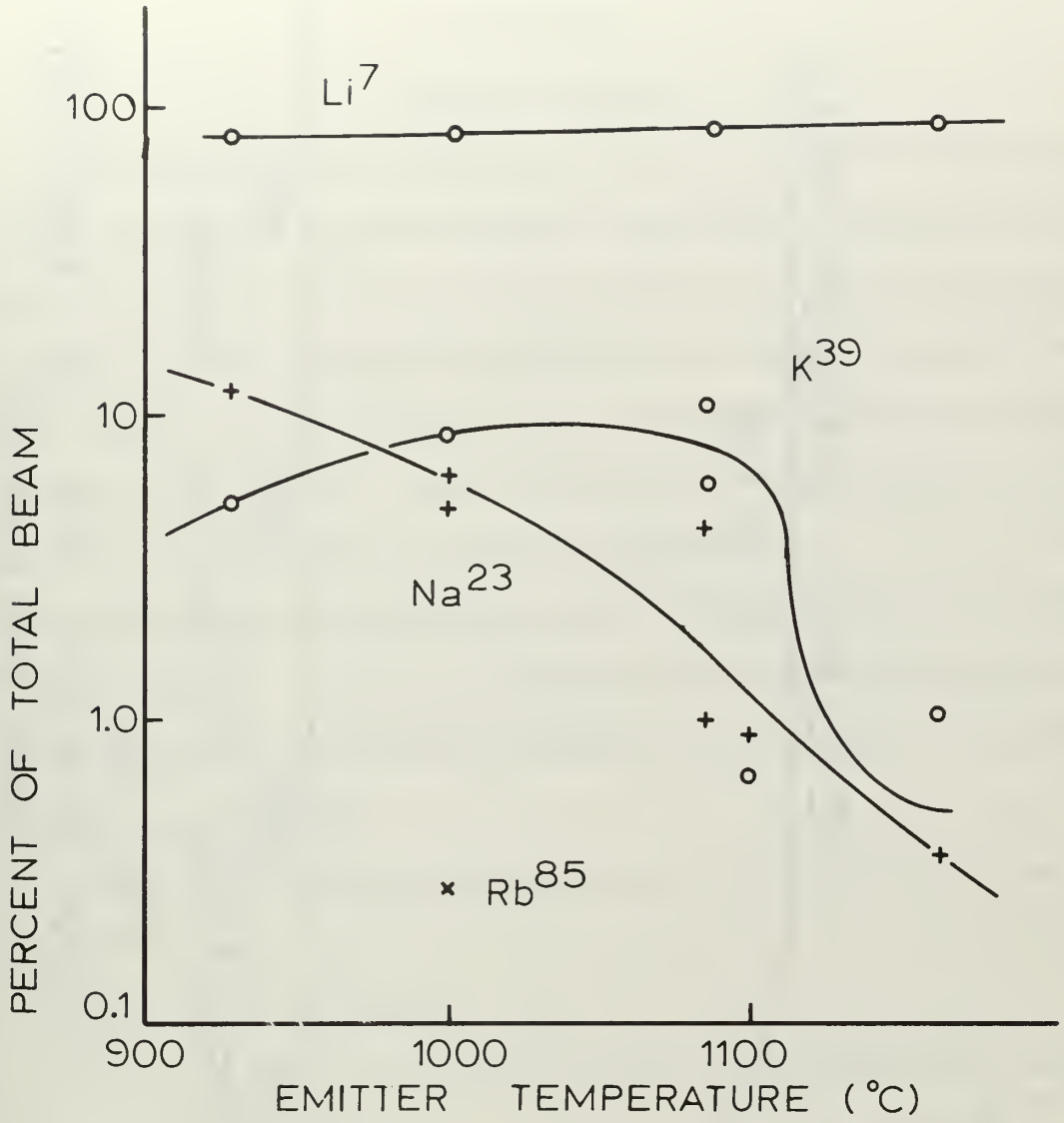


FIG. 31.*

LITHIUM SOURCE MASS ANALYSIS

*Data furnished by Drs. W. Aberth and J. R. Peterson of Stanford Research Institute.

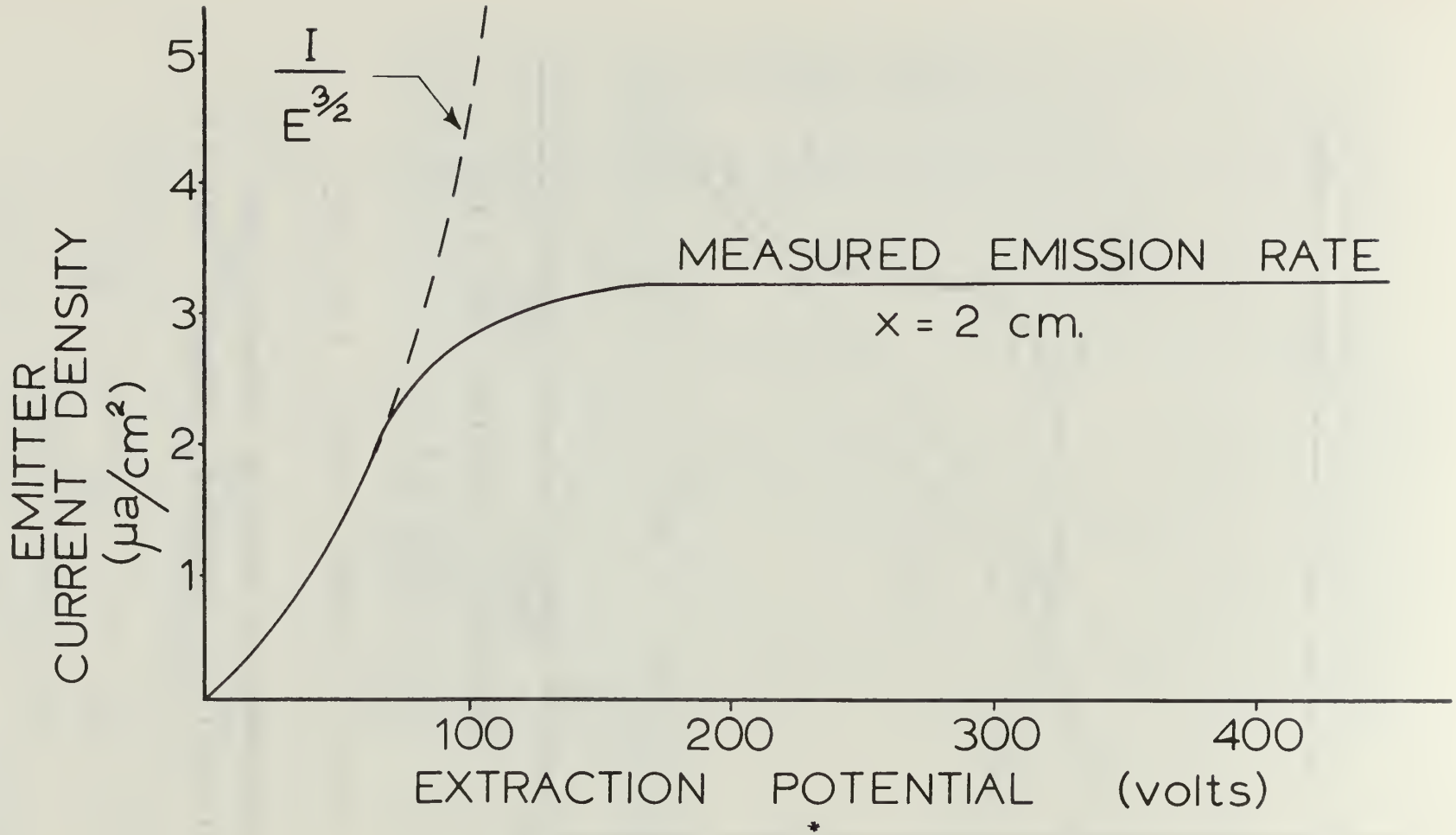


FIG. 32.*

DIODE EMISSION CHARACTERISTIC OF Li^+ EMITTER

*Data from Haskell[15]

CHAPTER VI

DISCUSSION

I. GAS ION SOURCES

The duoplasmatron and electron impact gas ion sources, like all other low energy ion beam devices, are severely affected by the forces or space charge. For both sources, the electrostatically focused ion beams sensed in DETECTOR are within a factor of two of the theoretical space charge limited ion beam which can be produced in our geometry. The calculation of space charge limited currents for ion beams is shown in Appendix C.

Several basic differences between the two sources are treated in this chapter. Table 1 is given by way of comparing quantitatively a number of parameters involved (lithium source included).

Ionization Efficiency

Three mutually dependent parameters determine the formation of ions in a plasma:

(a) electron energy

(b) the mean free paths of electrons between collisions with gas neutrals

(c) the probability of ion formation, or the ionization cross section.

Electron energy and mean free path length are influenced by the plasma density, which also controls the process of ion-electron recombination which removes ions from the plasma. Plasma density, in turn, is a function of source gas pressure and arc (grid) current, directly related to the arc (grid) potential. In the duoplasmatron, magnetic constriction additionally modifies the plasma density. The

third parameter, ionization probability, is a function of the other two, as well as the ionization potential of the gas. We know that an electron which collides with a gas atom must have an energy $K \geq eV_i$ in order to be able to ionize the atom. An electron with smaller energy has no likelihood of ionization, hence we should expect the ionization probability curve to rise sharply from zero at $K = eV_i$.

Thus the result is obtained that the yield of positive ions in our two gas sources is nominally a function of arc (grid) voltage and source gas pressure. The interaction of these independent variables can be described by a single parameter, ionization efficiency. The usual definition of ionization efficiency is the number of ion pairs which a primary electron will produce per cm of path at a pressure of 1 torr and at $0^{o}C$. The anticipated and empirical shape of the ionization curve displays a steep, nearly linear rise from zero; a maximum, whose location is determined by optimum values of parameters (a), (b), and (c) above; and a decrease at electron energies greater than about 3-5 eV_i.

In our two gas sources ionization takes place in the linear region between threshold and peak ionization efficiency. The ionization efficiency in this range can be expressed as $s_e = a\ P\ (eV - eV_i)$ ion pairs/cm/primary electron where (a) is a constant expressed in the proper units, P is pressure expressed in torr, and V is the arc (grid) voltage given in volts. Von Engel's[5] values for (a) are:

He	4.6×10^{-2} ion pairs/cm torr volt
H_2	21×10^{-2} ion pairs/cm torr volt

In the duoplasmatron the maximum arc voltage amounts to about 80 volts at a discharge chamber pressure of 0.2 torr. The maximum energy available to an electron in the electron impact source is the grid voltage (100 v), at pressures of 4×10^{-3} torr. The ionization potential for hydrogen is 15.4 eV, and the ionization efficiencies are

$$s_{e\ (duo)} = 21 \times 10^{-2} \times 0.2 \times (80-15.4) = 2.71 \text{ ionizations/cm}$$

$$s_{e\ (e.i.)} = 21 \times 10^{-2} \times 4 \times 10^{-3} \times (100-15.4) = 0.07 \text{ ionizations/cm}$$

Principally due to higher gas operating pressure, then, the duoplasmatron ionization efficiency greatly exceeds that of the electron impact source. This advantage appears in much lower electron flux, hence cathode power, requirements. Values are given in Table 1.

Gas Consumption

Conventional gas flow through an orifice occurs at pressures such that collisions between molecules take place more frequently than collisions of molecules with the walls of the aperture. This flow is described as viscous and is analyzed hydrodynamically. The properties of the gas (temperature, pressure, and flow velocity) do not vary over one mean free path of a particle and the gas can be considered to be a continuous medium.

Molecular flow takes place at very low pressures (P), when the mean free path (λ) is large compared to the characteristic dimension (orifice radius r) of the aperture, and gas flow is limited by molecular collisions with the walls of the channel. Flow rate is determined by geometrical analysis of the restrictive effect of the orifice on the free flight of molecules.

Dushman[6] defines molecular flow as that which exists when the parameters

$$\lambda/r > 1.00$$

$$rP \lesssim 5.0 \quad (r \text{ in cm, } P \text{ in microns})$$

From values given by Dushman the mean free paths of H_2 molecules in the duoplasmatron and electron impact ion sources can be calculated for operating conditions, which are also shown:

	Duoplasmatron	Electron Impact Source
λ	0.046 cm	2.33 cm
r	0.0254 cm	0.25 cm
P	200 microns	4 microns

Hence,

λ/r	1.8	9.17
rP	5.08	1.00

Flow is molecular in both sources.

Flow rate Q is defined as the product of the volumetric flow rate dV/dt across a plane and pressure P:

$$Q = P\ dV/dt = kT\ \ dN/dt \qquad \text{(VI.1)}$$

From the ideal gas law and equation (VI.1) the molecular flow through an orifice is

$$Q = \tfrac{1}{4}\ \bar{v}\ A\ (P_2 - P_1) \quad \text{(micron liters/sec)} \qquad \text{(VI.2)}$$

where $\bar{v}$ = mean molecular speed $= \left(\frac{8kT}{\pi m}\right)^{\frac{1}{2}}$

A = orifice area

P_2 = arc chamber pressure

P_1 = pressure outside chamber

In both ion sources, $P_2 >> P_1$, and the approximation $(P_2-P_1) = P_2$ can be made. Equation (VI.2) applies for practical purposes when the radius of the orifice satisfies the previous requirement for molecular flow, that is $\lambda/r \gtrsim 1.00$.

Comparing the flow rates of the two sources at operating pressures,

$$\frac{Q \text{ (electron impact source)}}{Q \text{ (duoplasmatron)}} = \frac{r_e^2 P_e}{r_d^2 P_d} \approx 2$$

Hence, in the manner in which the two sources are operated (producing ion beams of like intensity) the electron impact source requires about twice as much gas as the duoplasmatron. Quantitative measurements have not been made.

Cathode Life

It is important to note the structual differences between the cathodes in the two ion sources, as this figures in cathode life expectancy. The potential drop across the cathode gives rise to a temperature gradient. As is discussed in detail in Appendix B, the temperature gradient in the duoplasmatron filament is marked, and is a direct cause of deterioration and failure. The use of a hairpin configuration ensures that the small terminal potential drop (1.1 volt) of the filament is confined to a highly localized emission region at the tip. Evidence of this is obtained from the fact that all failed filaments (2 hours at worst) have separated at this point. The cathode of the electron impact source, on the other hand, consistently has a longer average operating life ($>$ 100 hrs) in spite of a higher power usage ($\sim$ 200 watts). This is probably due to a more even temperature distribution, since the tungsten wire is of uniform cross section configured in a coil to avoid localized emission regions.

Minor Maintenance

Both ion sources require occasional housekeeping maintenance. The arc chamber of the duoplasmatron collects most of the steadily deteriorating filament (see Appendix B) and care must be taken to guard against fragments plugging up the anode aperture. The aperture itself suffers continual ion and electron bombardment from the arc and shows some pitting. It is possible that replacement will be necessary after about 500 hours of operation. The einzel lens remains particularly clean due to (i) the fact that the anode receives the brunt of the arc energy, and (ii) the relatively large lens apertures (the exiting ion beam appears to clear L_1 almost entirely).

Contaminated lenses are the principle clean-up problem of the electron impact source, due to a larger anode aperture and more exposed focus stack. The gradual accumulation of an oil coating from the vacuum pumping system conspires with the ion beam to build up charge on the lens surfaces. To remedy this the surfaces are painted with a commercially obtainable colloidal suspension of graphite in water, sold as Aquadag. The graphite layer buckles and flakes away after 20-30 hours of source operation, and the lenses require cleaning and repainting.

II. LITHIUM ION SOURCE

The lithium ion source has a number of attractive advantages over the complex gas ion sources. Foremost are simplicity of construction and operation. In addition, the lithium source produces a very well defined, nearly monoenergetic ion beam, which is essentially devoid of impurities. The beam has far greater stability

than that of either gas ion source. The filament power consumption is intermediate (90 watts as compared to 11 watts for the duoplamatron and ~ 200 watts for the electron impact source), but the source requires only one other power supply for operation, that for beam acceleration. The theory of operation of the lithium source can be applied to nearly all alkali metals, and several other mineral compounds have been developed for thermal ion sources.

Probably the most serious drawback of the lithium ion source is the fact that it is emission limited at beam energies above 200 eV (see Fig. 32). It has been pointed out that space charge exists as a fundamental limit on the beam intensity available by any single-stage ion source operating at low energies. Experimental data for the lithium source indicates that below 200 eV the ion beam is limited by space charge, but at higher acceleration potentials it becomes emission limited. At energies of 200-500 eV beam intensities are reduced to less than those predicted by space charge theory by a factor averaging about 30.

To see how emission limitation in the lithium source comes about, we must look at the voltage law for plane surfaces, as obtained by Child[7]. This can be expressed as

$$I = \text{const.} \times \frac{E^{3/2}}{d^2} \quad \text{amps/cm}^2 \qquad \text{(VI.3)}$$

where I = beam current, E = beam energy, d = emitter-extraction probe distance. The relation is developed assuming the ions leave the emitter with no initial velocity. In practice this ideal is not realized, as ions emerge from the source with velocities ranging from zero upwards. If the assumption is made that Maxwell's distribution

law governs particle energies inside the emitter, corresponding to temperature, theoretical considerations dictate that the law apply to ions outside the emitter as well. Statistical mechanics confirm this contention.

The space current, when limited by space charge, differs from that given by equation (VI.3) as the initial velocities of emission and beam accelerating potentials grow. The effect is shown in Fig. 33.

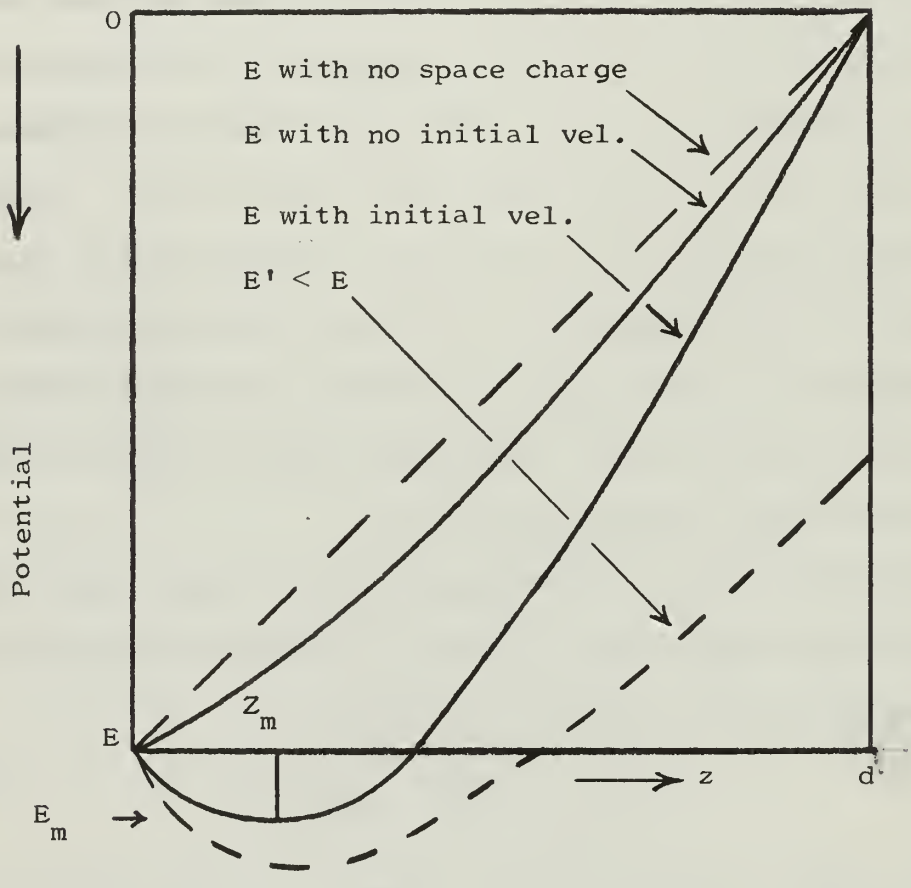


Fig. 33

Variation of potential between plane parallel electrodes showing effect of initial velocity of emission.

If the emitted ions have initial velocities of Maxwellian distribution, there is a region in front of the emitter where the potential is positive with respect to the emitter, and a maximum potential E_m occurs at a distance z_m from the source. The force per unit charge is given by the slope of the potential, so the axial electric field force on ions at $z < z_m$ is negative and toward the emitter. At $z = z_m$ the force is zero, and for values of $z > z_m$ the force is toward the extracting lens (ground). Under steady state conditions with a continuous flux of ions, the electric field tends to force ions away from z_m in both directions and minimize the average velocity. This relates to maximizing radial space charge effects at z_m. The effect is that of a diverging electrostatic lens, and z_m corresponds to its position along the ion beam path. It is clear that the closer z_m is to the face of the source, the more degrading the result will be upon ion beam intensity.

Wehnelt and Bley[7] have measured the distribution of potential between numerous emitters and extraction plates and find that z_m and E_m decrease with an increase in accelerating voltage. The result of decreasing z_m is to accentuate the destructive effect, while decreasing E_m reduces it. Since emission limitation is observed in the lithium ion beam, it appears that the adverse influence of making z_m small is greater than its countereffect, reducing E_m.

The lithium ion source emission problem must be considered more or less unavoidable, since a Maxwellian velocity distribution of ions is temperature dependent and therefore always present. It is hoped that thermal effects can be partially reduced by the

development of emitters which will operate at lower temperatures. Emitter improvement over pioneer types has thus far not given this result, but by increasing the porosity of the tungsten disc in which the β-eucryptite is imbedded, the quantity of lithium available has been increased and the life of the source prolonged.

TABLE 1.

COMPARISON OF ION SOURCES

PARAMETER	DUOPLASMATRON	ELECTRON IMPACT SOURCE	LITHIUM SOURCE
Ion beam available	H^+, H_2^+, H_3^+, He^+, N^+, N_2^+, and other gases variety of negative ions		L_i^+ (mass 6 or 7) source can be adapted to other alkali metals
Source of ions	electron impact ionization		thermal emission from mineral alkali metal
Ion beam intensity (75 cm downstream)	0.2 $\mu a/cm^2$	0.2 $\mu a/cm^2$	0.1 $\mu a/cm^2$
Beam energy range investigated	V_i - 500 eV	V_i - 500 eV	0-500 eV
Beam energy dispersion	2-3% of beam energy	~2 eV*	tenths of eV
Gas pressure in arc chamber	0.2 torr	4×10^{-3} torr	n/a
Relative gas consumption	x 1	x 2	n/a
Ionization efficiency	2.1 $\frac{\text{ion pairs}}{\text{electron cm}}$	0.07 $\frac{\text{ion pr.}}{\text{elec cm}}$	n/a
Filament power	11 watts	150-250 watts	80-90 watts
Filament temperature	700°C	1800-2000°C	1150°C
Filament life	100 hrs	> 100 hrs	> 100 hrs
Arc current	0.2-1.1 amps	75 ma	n/a
Arc voltage	50-80 volts	100 volts	n/a
Ion beam focusing	einzel lens	einzel lens	einzel lens

* furnished by D.C. Lorents and W. Aberth of SRI.

BIBLIOGRAPHY

1. George H. Strohsahl, thesis, NPGS, 1967.

2. W. Aberth and J.R. Peterson, scientific note, Stanford Research Institute, 1966.

3. G.P. Lawrence, R.K. Beauchamp, and J.L. McKibben, Nucl. Instr. and Meth. 32, 357 (1965).

4. H.B. Haskell, O. Heinz, and D.C. Lorents, Rev. Sci. Instr. 37, 607 (1966).

5. A. Von Engel, Ionized Gases (Clarendon Press, Oxford, 1965).

6. Saul Dushman, Scientific Foundations of Vacuum Techniques (John Wiley & Sons, New York, 1962), pp. 30-117.

7. E. Leon Chaffee, Theory of Thermionic Vacuum Tubes (McGraw Hill, New York, 1933), pp. 55-114.

8. P. Grivet, Electron Optics (Pergamon Press, Oxford, 1965), pp. 277-283.

9. C.J. Cook, technical report, SRI, 1959.

10. D.R. Bates, ed., Atomic and Molecular Processes (Academic Press, New York, 1962), Ch. 11.

11. Sanborn C. Brown, Introduction to Electrical Discharges in Gases (John Wiley & Sons, New York, 1966).

12. Harold P. Eubank, Russell A. Peck, and Rohn Truell, Rev. Sci. Instr. 25, 989 (1954).

13. John Fasolo, engineering note, University of California, 1957.

14. L.M. Field, Rev. Mod. Phys. 18, 353 (1946).

15. Hugh B. Haskell, thesis, NPGS, 1965.

16. O. Klemperer, Electron Optics (University Press, Cambridge, 1953), Ch. 8.

17. W.A. Lamb, E.J. Lofgren, Rev. Sci, Instr. 27, 907 (1956).

18. Earl W. McDaniel, Collision Phenomena in Ionized Gases (John Wiley & Sons, New York, 1964).

19. C.D. Moak, H.E. Banta, J.N. Thurston, and J.W. Johnson, Rev. Sci. Instr. 30, 694 (1959).

20. O.B. Morgan, G.G. Kelly, and R.C. Davis, Rev. Sci. Instr. 38, 467 (1967).

21. J.R. Pierce, Theory and Design of Electron Beams (Nostrad Co., Inc, New York, 1954), Ch. 6,9.

22. R.H. Prince, technical note, University of Toronto Institute for Aerospace Studies, 1965.

APPENDIX A

THEORY OF IONIZATION AND GASEOUS DISCHARGE PERTINENT TO ION SOURCE OPERATION

A source of primary electrons, in the presence of an electric field and a gas, can be made to produce gaseous discharges by electron-molecule collisions. A natural division exists between those discharges which are self-sustaining and those which are not. In the duoplasmatron and the electron-impact ion sources the heated filament provides the primary electron flux and is required to maintain the arc. Hence, both discharges can be classified as thermionic arcs with external cathode heating, and non-self-sustaining.

For this development, consider two parallel electrodes with separation d, one of which is emitting electrons. When a gas at constant pressure is introduced and an increasing electric field is applied between the electrodes, anode current grows until saturation is achieved, that is, all electrons emitted thermionically from the cathode reach the anode. The current-voltage relationship is shown in Fig. 34. As voltage is increased above that required to produce saturation, the current again increases, slowly in region T_1, and then rapidly in region T_2, the Townsend discharge regions. The behavior in the first Townsend region is due to ionization of neutral molecules by primary electrons which have gained sufficient energy from the electric field. The first Townsend coefficient α describes the number of new ion pairs produced per cm. of path by an accelerated electron, and is inversely proportional to the mean free electron path. In region T_2, secondary electrons are emitted from the cathode due to positive ion bombardment (γ electron/incident ion), and discharge current increases accordingly. In self-sustaining

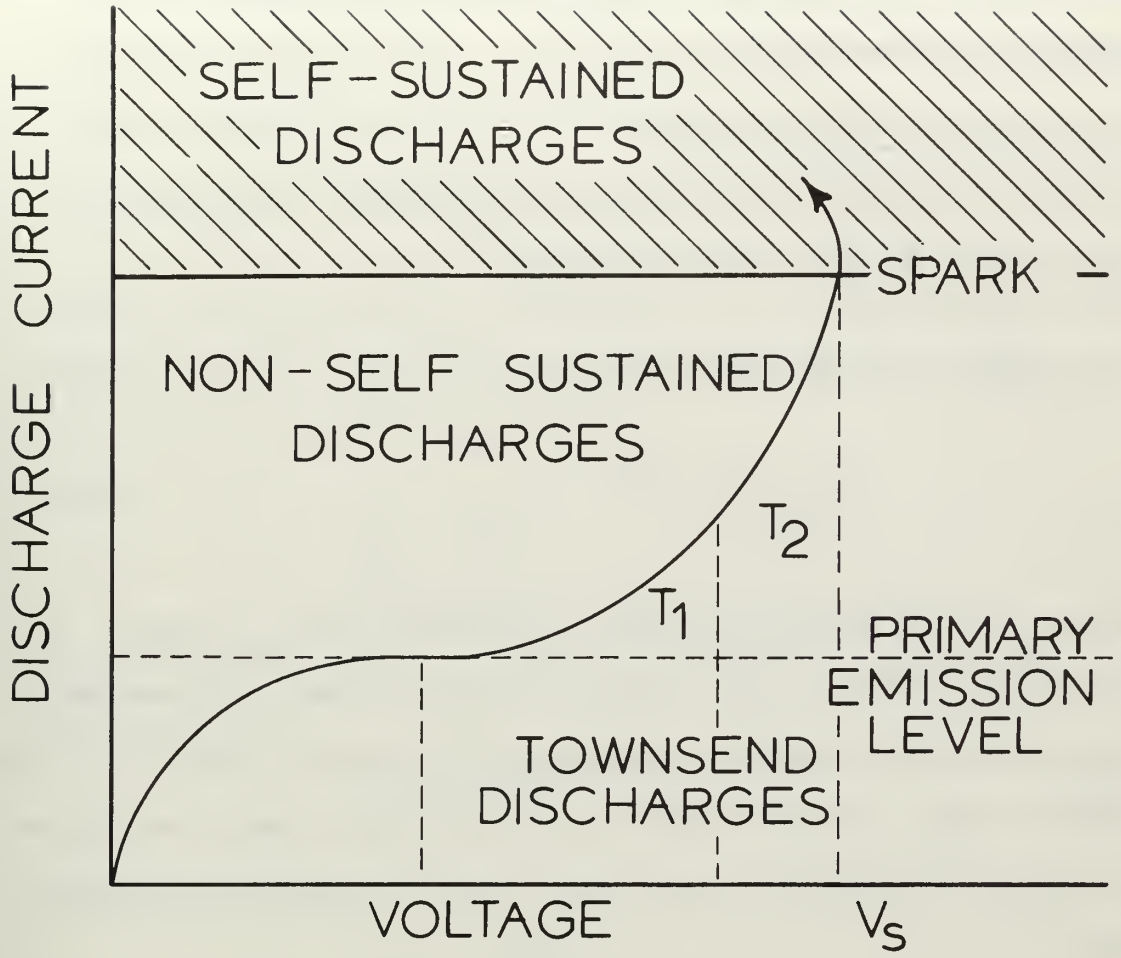


FIG. 34.

ELECTRICAL DISCHARGES
IN GASES

region the secondary electron population is maintained in the absence of cathode heating.

Ionization in a Uniform Field

In the parallel plate geometry, for $d \gg \lambda$, the increase in ion pairs in dx is α dx per electron:

$$dn = n \alpha \, dx \tag{A.1}$$

$$\frac{n}{n_o} = \frac{i}{i_o} = e^{\alpha d} \tag{A.2}$$

where n_o is the number of primary electrons, and i_o is the saturation current. If n_c represents both primary and secondary electron emission from the cathode, and n electrons reach the anode, then the number of ions formed in the gas which reach the cathode is $(n-n_c)$. The number of secondary electrons emitted is $\gamma(n-n_c)$. Hence

$$n_c = n_o + \gamma(n-n_c) \tag{A.3}$$

or

$$n_c = \frac{n_o + \gamma n}{1 + \gamma} \tag{A.4}$$

Current is amplified according to equation (A.2), so that the total number of electrons (and subsequent current) reaching the anode is

$$n = n_c \, e^{\alpha d} \tag{A.5}$$

$$\frac{n}{n_o} = \frac{i}{i_o} = \frac{e^{\alpha d}}{1-\gamma(e^{\alpha d}-1)} \tag{A.6}$$

It is important to investigate the behavior of anode current with varying gas pressure. In order to ionize at collision, an electron having traveled path length ℓ must have energy

$$eE\ell \geq e V_i \tag{A.7}$$

(where E is the electric field intensity, v/cm) hence the requirement $\ell \geq V_i/E$ in the field direction. The relative number of electrons having $\ell \geq \lambda$ is given by

$$\frac{n}{n_o} = e^{-\ell/\lambda} \tag{A.8}$$

The probability per cm path of an ionization taking place is then described by

$$\alpha = \frac{1}{\lambda} e^{-\ell/\lambda} \tag{A.9}$$

Imposing $\ell = V_i/E$

$$\alpha = \frac{1}{\lambda} e^{-\frac{V_i}{E\lambda}} \tag{A.10}$$

Letting $A = 1/\lambda_1$, $B = V_i/\lambda_1$, $\lambda = \frac{\lambda_1}{p} = \lambda_1$ when $p = 1$, we have

$$\frac{\alpha}{p} = A e^{-\frac{Bp}{E}} \tag{A.11}$$

Therefore,

$$\frac{\alpha}{p} = f\ (E/p) \tag{A.12}$$

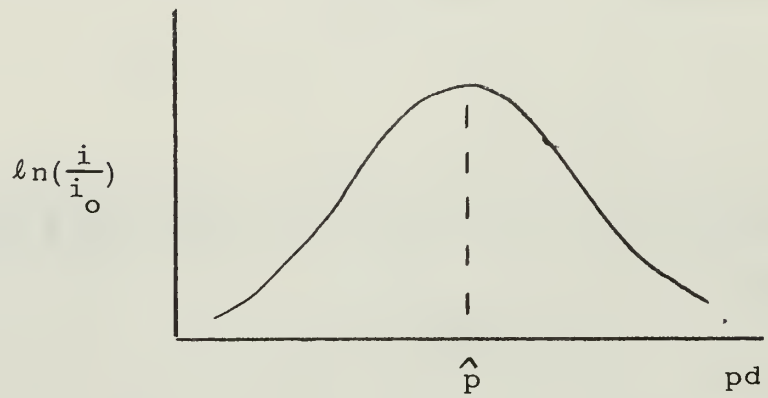
The constants A and B have been determined empirically. The sigmoid curve described by (A.10) shows departures from observations arising from failure to account for elastic collisions, and the assumptions

that no electrons gain more energy than eV_i, and that once an electron has acquired that energy the probability of ionization equals 1.0.

From equations (A.2) and A.10), remembering that E = V/d,

$$\ell n\left(\frac{i}{i_o}\right) = \alpha d = (pd)\, Ae^{-\frac{B(pd)}{V}} \qquad (A.13)$$

which is pictured roughly:



The maximum appears because at low gas density, λ is large and ionizing collisions are few. At high pressures, λ is smaller and often $eE\ell < eV_i$, hence only electronic or molecular excitations take place. The maximum can be found:

$$\frac{d(\ell n\ i/i_o)}{d(pd)} = 0$$

and results in

$$\hat{pd} = \frac{V}{B} \qquad (A.14)$$

Starting Potentials and Breakdown

From (A.6) and (A.12) it can be seen that at a certain critical value of E/p current multiplication becomes infinite. In

practice, a finite power source limits (A.6), but the solution to $\gamma(e^{\alpha d}-1) = 1$ yields the breakdown field or sparking voltage in terms of the gas pressure, the gas, and d. From (A.11),

$$\gamma\left(e^{\frac{\alpha}{p}(pd)} - 1\right) = 1 \qquad \text{(A.15)}$$

$$\gamma\left(e^{(pd)\,Ae^{-\frac{Bp}{E}}} - 1\right) = 1 \qquad \text{(A.16)}$$

Solving yields

$$\frac{Bp}{E} = \ell n(pd) + \ell n \frac{A}{\ell n(1+\frac{1}{\gamma})} \qquad \text{(A.17)}$$

$$c$$

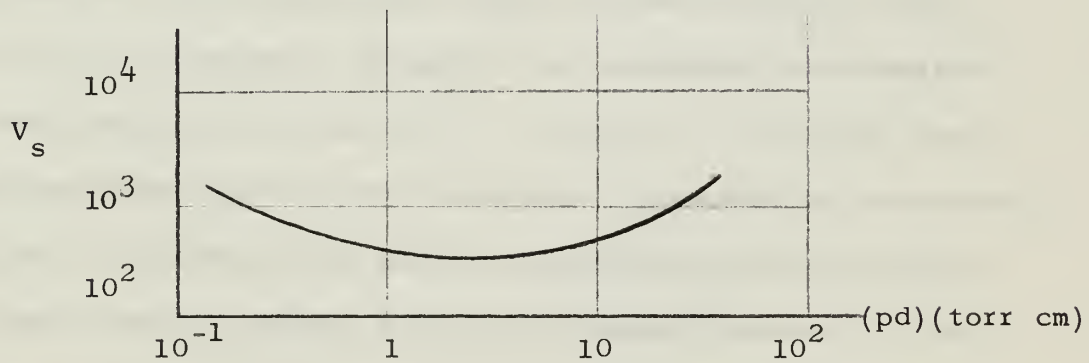
or

$$\frac{Es}{p} = \frac{B}{\ell n(pd) + C} \qquad \text{(A-18)}$$

which becomes

$$V_s = \frac{B(pd)}{\ell n(pd) + C} \qquad \text{(A.19)}$$

and is shown below for hydrogen.



The behavior is predictable. At low (pd), α is small and most of the electrons collide with the anode. At relatively high pressures, λ is small and few electrons acquire sufficient energy to ionize.

APPENDIX B

CATHODE ELECTRON EMISSION OXIDE-COATED

It is well established that oxide-coated, unipotential cathodes at comparatively low temperatures give copious emission of electrons. Nowadays the use of barium, strontium, and calcium carbonates has been standardized. The "triple carbonate" consists of a mixture of 57-4-39 parts by weight of $BaCO_3$, $CaCO_3$, and $SrCO_3$, dissolved into a thin fluid paste of amyl acetate, and can be obtained commercially.

The mechanism of electron emission from an oxide-coated cathode is not fully understood, though it is established that the source metal is a thermally or otherwise reduced monatomic layer of the several species which resides on the outer oxide surface, the oxide serving only as a reservoir for the metals. High emission can be attributed to the low work function of these metals and the effect of single atomic layers which aid the escape of electrons.

Oxide coatings are classified as either combined or uncombined types. The filament is coated and heated in air at $700^{\circ}C$ in the former, and nickelates are formed by combination of the nickel filament core with the oxides. In the uncombined class, the coated cathode is dried in a vacuum or low pressure hydrogen atmosphere, and the oxide cover merely resides on the filament. In either case, initial heating drives off CO_2 and leaves the metal oxide. The combined filaments have a darker appearance than the uncombined types.

The oxides themselves do not emit electrons, but must first be activated, or reduced to neutral metal. The activation mechanism has not been clearly established, but existing opinions can be

classified under reduction by (1) electrolysis, (2) positive-ion bombardment, and (3) thermal disassociation.

In the process of electrolysis, conduction of source current electrons (hot cathode) through the oxide layer frees the metal from its oxide, reducing some of the metal on the spot ($BaO + e \longrightarrow Ba^{+} + O^{--}$, $BaO + 2e \longrightarrow Ba + O^{--}$, etc.). The remaining positively charged ions are transported to the negative cathode and reduced there. The neutral metal atoms then diffuse outward to the outer oxide-layer surface, due to high filament temperature. Some oxygen is liberated at the surface as well. Uncombined metal has been detected at both the inner and outer surfaces of cathodes of this type, lending credence to this theory.

It has been calculated that by bombardment of the coated cathode, positive ions with energies of $\sim$ 100 eV are energetic enough to break down BaO and SrO into metal atoms and oxygen. Unexplained by this reduction theory are how initial activation takes place and how this process in a high vacuum can maintain a sufficient metal monolayer on the oxide surface. Once the duoplasmatron is operating, it is clear that reduction by bombardment assists activation.

Thermal reduction possibly occurs by disassociation of the metal oxides by heat, or displacement of Ba, Sr, and Ca by chemically active nickel in the presence of extreme temperatures.

There is evidence that the activation of oxide coated filaments is a combination of the three processes, namely: the chemical compounds forming the coating supply active metals which are reduced by electrolysis and ion bombardment to neutral metals. Thermal

disassociation may take place. Neutral metal atoms diffuse outward to the surface of the oxide coat, adhering most likely to a thin, monatomic film. Emission takes place primarily from the metal film, secondarily from free atoms within the coating. As reduction occurs oxygen is liberated; perhaps this underlayer serves to reduce the metal work function. The metals evaporate and require replenishing, which is accomplished by continuous electrolysis during operation.

Thermal electron emission from a clean, homogeneous surface is a well-known phenomenon, described by

$$j = AT^2 e^{-\phi_o/kT} \tag{B.1}$$

where j = current density (amp/cm^2)

A = material constant (amp/cm^2 ^oK)

T = Kelvin temperature

ϕ_o = metal work function (volts)

For the complex cathode involving several metals, empirical relationships must be determined. Emission characteristics for oxide-coated cathodes have been studied and given as

$$j = C e^{-\phi_o/kT} \tag{B.2}$$

where C is a thermionic constant that is determined for each emitter to fit the observed data. The measurement of emission constants for oxide-coated cathodes is made difficult by the fact both C and ϕ_o decrease as activation proceeds. This progressive

change, together with the fact that oxide-coated cathodes show no marked saturation, leads to a variety of calculated values. The generally accepted value for ϕ_o for CaO + SrO + BaO is 1.24 volts.

In practice, emission density is determined by the cathode life required and by space charge limitations. It is fruitless to heat the filament beyond temperatures at which space charge limited ion beams are produced. Deleterious effects encountered by heating are flaking of the oxide coating and filament burnout. Flaking can occur by overheating or cathode poisoning. The heating characteristics of the oxide coat cause hot spots to arise in thicker portions of the coat. In additional, the space current entering the cathode (electrons leaving) is superimposed upon the heating current, making the actual current in the filament vary along its length. Hence temperature displays variation throughout the filament, and in turn alters the emission, resistance, and potential gradient. All these various effects are mutually dependent and cause flaking and burnout. During this study, numerous filaments failed by melting, and all failures were attributed to excessive operating or spurious temperatures.

Cathode poisoning is the term given to a process identical to the ion-bombardment reduction phenomenom discussed earlier. Under bombardment by positive ions, mechanical deterioration and flaking of the oxide surface takes place. It is unavoidable in the duoplasmatron, and is actually an assist in maintaining low cathode power requirements by keeping the filament hot. Flaking was observed in all filaments constructed for the duoplasmatron.

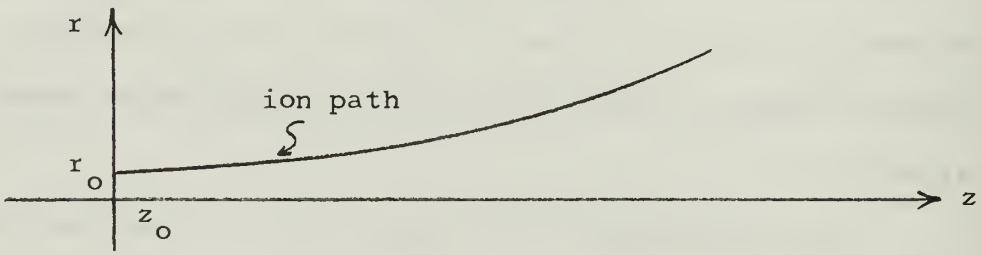
In addition, cathode life is limited by the loss of emission properties due to slow evaporation of the metal supply. To retard this loss the oxide coating is made as thick as possible on new filaments.

APPENDIX C

SPACE CHARGE THEORY

Mutual electrostatic repulsion between ions of like charge in a beam prevents the beam from being focused, and causes divergence throughout its path. The broadening of the beam is comparable with that due to a weak, unadjustable divergent lens.

By making several assumptions, the general differential equation for the path of an ion in an electrostatic field of rotational symmetry can be obtained from the fundamental equations of motion. The assumptions made are (i) that the radial current density is constant across any beam cross section and zero outside the outer rays, (ii) the total current is constant, and (iii) the divergence of the beam is sufficiently small to approximate zero force in the axial direction and constant axial velocity. Considering the geometry below:



the ion's velocity is given by

$$v \approx \frac{dz}{dt} = \sqrt{\frac{2eV}{M}} \qquad (C.1)$$

The radial electric field can be calculated by applying Gauss' Theorem to a small cylinder with axiz z, length dz, and radius r. The flux through the surface is

$$\Phi = \vec{E} \cdot d\vec{S} \qquad (C.2)$$

where

$$\int \vec{E} \cdot d\vec{S} = \frac{\rho \pi r^2 dz}{\epsilon_0} \tag{C.3}$$

$$E_r (2\pi r\, dz) = \frac{\rho \pi r^2 dz}{\epsilon_0} \tag{C.4}$$

$$E_r = \frac{\rho r}{2\epsilon_0} \tag{C.5}$$

but

$$I = \pi r^2 \rho v \tag{C.6}$$

$$\rho = \frac{I}{\pi r^2} \sqrt{\frac{M}{2eV}} \tag{C.7}$$

$$E_r = \frac{1}{2\pi\epsilon_0} \frac{1}{r} \sqrt{\frac{M}{2e}} \frac{I}{\sqrt{V}} = \frac{M\ddot{r}}{q} \tag{C.8}$$

$$\ddot{r} = \frac{1}{2\pi\epsilon_0} \frac{1}{r} \sqrt{\frac{e}{2M}} \frac{I}{\sqrt{V}} = \frac{C'}{r} \frac{I}{\sqrt{V}} \tag{C.9}$$

$$\frac{d^2r}{dt^2} = \frac{d^2r}{dz^2} \left(\frac{dz}{dt}\right)^2 = \frac{C'}{r} \frac{I}{\sqrt{V}} \tag{C.10}$$

Remembering that the axial motion is uniform,

$$\frac{d^2r}{dt^2} = \frac{1}{4\pi\epsilon_0} \frac{1}{r} \sqrt{\frac{M}{2e}} \frac{I}{V^{3/2}} \tag{C.11}$$

$$= \frac{1}{r} \left(\frac{\beta}{2}\right) \tag{C.12}$$

where

$$\beta = \frac{1}{2\pi\epsilon_0} \sqrt{\frac{M}{2e}} \frac{I}{V^{3/2}} \tag{C.13}$$

Multiplying (C.11) by dr/dz, and integrating:

$$\left(\frac{dr}{dz}\right)^2 = \beta \ln \frac{r}{r_0} \tag{C.14}$$

We make the substitution

$$\varepsilon^2 = \ln \frac{r}{r_0} \tag{C.15}$$

and solve for r:

$$r = r_0 e^{\varepsilon^2} \tag{C.16}$$

Differentiating, and making use of (C.14),

$$\frac{dr}{dz} = 2r_0 e^{\varepsilon^2} \varepsilon \frac{d\varepsilon}{dz} = \sqrt{\beta}\ \varepsilon \tag{C.17}$$

Upon integration

$$z - z_0 = \frac{2r_0}{\sqrt{\beta}} \int_{\varepsilon_0}^{\varepsilon} e^{\varepsilon'^2} d\varepsilon' \tag{C.18}$$

we isolate the Dawson function, which has been tabulated:

$$D(\eta) = \int_0^{\eta} e^{\varepsilon'^2} d\varepsilon' \tag{C.19}$$

We may finally write

$$z - z_0 = \frac{2r_0}{\sqrt{\beta}}\ D\left(\sqrt{\ln \frac{r}{r_0}}\right) \tag{C.20}$$

which represents the trajectory of the outer ray in a beam which constantly diverges.

By way of illustration, consider the duoplasmatron mounted in our geometry with hydrogen gas being used. Allow that an ion beam originates in the anode aperture and is accelerated to a detector of 0.5 cm radius and 75 cm away. This will predict the approximate space charge limited current which can be obtained. Focusing and magnetic field effects might be expected to enhance the beam intensity by a factor of ~ 2.

The dimensions are:

$$r_o = 2.54 \times 10^{-2} \text{ cm}$$

$$r = 0.5 \text{ cm}$$

$$z - z_o = 75 \text{ cm}$$

From Grivet[8],

$$D\left(\sqrt{\ell n\, r/r_o}\right) = 7.0$$

From (C.13), for H^+ we have

$$\beta = 3.26 \times 10^5 \, I/E^{3/2}$$

From (C.20) we obtain

$$\beta = 2.248 \times 10^{-5}$$

Solving for I for a beam energy of 200 eV, we arrive at

$$I = \frac{(2.248 \times 10^{-5})(2825)}{3.26 \times 10^5} = 0.195 \, \mu a$$

This intensity is consistent with experimental results.

APPENDIX D

ENERGY ANALYSIS

All energy measurements made for this study were obtained using a 127.3^{o} cylindrical energy analyzer. The device, its operation, and use in our geometry are discussed in full by Strohsahl[1]. The basic theory of operation is treated by Cook[9], who gives the analyzer transmission function as

$$\frac{T(E-E')}{E} = \frac{4}{3}\alpha^2 + \frac{1}{2}\left(\frac{\ell_1 + \ell_2}{\pi r_o}\right) + \left(\frac{w_1 + w_2}{r_o}\right) \qquad (D.1)$$

where E = nominal beam energy at analysis

E' = energy variable

α = angular beam divergence

ℓ_1, ℓ_2 = length of entrance and exit slits

w_1, w_2 = width of entrance and exit slits

r_o = mean radius of the ion beam in the analyzer

Note that $\frac{T(E-E')}{E}$ is constant for a given geometry. Using a slit width of 0.05 cm, the transmission function has been calculated and is plotted in Fig. 35.

The current measured by the energy analyzer is dependent upon two parameters, the transmission function and the incident beam energy distribution, and can be interpreted as

$$I(E') = \int_o^\infty T(E-E')\, F(E)\, dE \qquad (D.2)$$

This amounts to integration of the product of (i) the beam energy function $F(E)$ which can normally be assumed to be a Gaussian distribution about the mean beam energy, and (ii) the transmission function which is the resolution of the energy analyzer, over all energies.

Equation (D.2) can be used to accurately interpret the energy spread of ion beams ($\Delta E = f(I(E'))$ as measured by our energy analyzer. The known quantities in this case are the transmission function (D.1) and the measured beam current at energy E'; the unknown is the beam energy distribution F(E). For the purposes of this paper, a simple graphical analysis was done.

Haskell, Heinz, and Lorents[4] performed energy measurements on a lithium beam at $E < 22.8$ eV, and found an energy dispersion of ~ 0.25 eV (full width at half maximum). Theory predicts that the energy spread of the ion beam should be of thermal origin only, and independent of beam energy. Empirical data taken with the cylindrical analyzer shows a beam energy spread at high accelerating potentials which is essentially linear with beam energy, and which varies from 2-5 eV in the range $100 < E < 500$ eV (see Fig. 35). A graphical solution of eq. (D.2) was found in order to test the validity of the theoretical energy distribution. F(E) for the lithium beam was assumed to be a Gaussian distribution with $\Delta E = 0.25$ eV, and the transmission function was symbolized by a triangle of base T(E-E'). This representation is considered valid since we know that the analyzer passes a beam of given nominal energy E and finite energy spread ΔE, but discriminates against ions in proportion to their deviation from the nominal beam energy (E-E'). The integral solution, I(E'), is represented by the product of (i) the area common to F(E) and the transmission function, and (ii) the height of the transmission function at E'. Figure 36 illustrates.

The graphical process was carried out for the lithium beam for energies $100 < E < 500$ eV, and the results (Fig. 35) are gratifyingly close to measured values. We can probably conclude that F(E) for the lithium beam at high energies is approximately like that at low energies, and that ΔE is on the order of one eV or less for all beam energies.

A more detailed study of the energy analysis of ion beams is beyond the scope of this paper. In theory, one could use empirical data and the relations found in eq. (D.1) and (D.2) to work back to exact descriptions of ion beam energy functions. Computer techniques would greatly facilitate this approach.

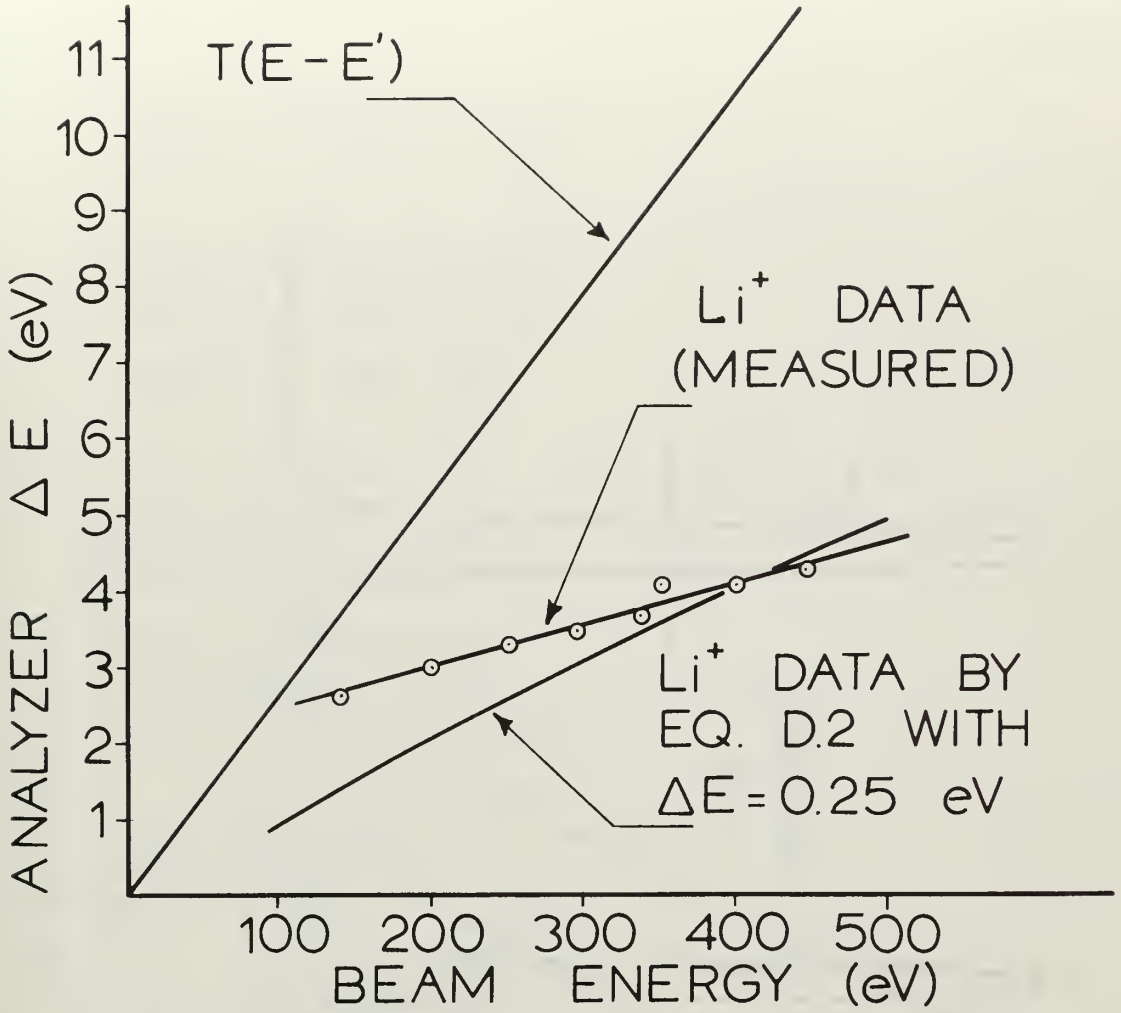


FIG. 35.

ANALYZER ENERGY SPREAD vs. BEAM ENERGY SHOWING TRANSMISSION FUNCTION & Li^+ DATA

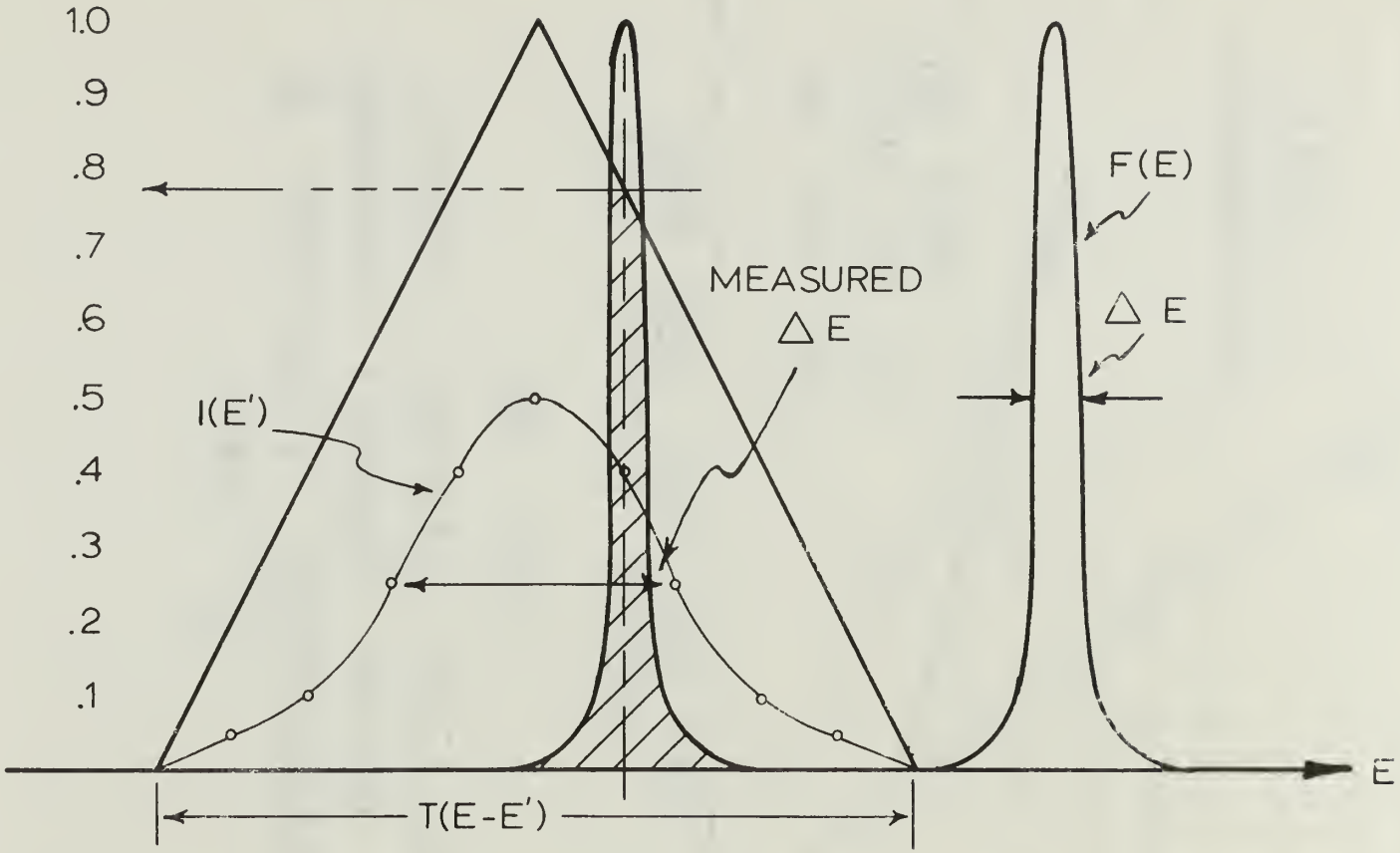


FIG. 36.

METHOD OF GRAPHICALLY OBTAINING

$$I(E') = \int_0^\infty T(E-E')\ F(E)\ dE$$

Initial Distribution List

		No. Copies
1.	Defense Documentation Center Cameron Station Alexandria, Virginia 22314	20
2.	Library Naval Postgraduate School Monterey, California 93940	2
3.	Commandant, USMC (A03C) Washington, D.C. 20830	1
4.	Prof. Otto Heinz Department of Physics Naval Postgraduate School Monterey, California 93940	3
5.	Capt. T.L. Carter, USMC Department of Physics Naval Postgraduate School Monterey, California 93940	2
6.	Lt. Thomas O. Bush, USN Department of Physics Naval Postgraduate School Monterey, California 93940	1
7.	Capt. N.R. Smyth, CAF Department of Physics Naval Postgraduate School Monterey, California 93940	1
8.	Mr. Thomas Maris Department of Physics Naval Postgraduate School Monterey, California 93940	1
9.	Defense Atomic Support Agency, Dept. of Defense Washington, D.C. 20301	1

DOCUMENT CONTROL DATA - R & D

(Security classification of title, body of abstract and indexing annotation must be entered when the overall report is classified)

1 ORIGINATING ACTIVITY *(Corporate author)*
Naval Postgraduate School
Monterey, California 93940

2a. REPORT SECURITY CLASSIFICATION
UNCLASSIFIED

2b. GROUP
N/A

3. REPORT TITLE
Ion Sources for the Production of Low Energy Beams

4. DESCRIPTIVE NOTES *(Type of report and inclusive dates)*
Thesis, MS, June 1968

5 AUTHOR(S) *(First name, middle initial, last name)*
Carter, Thomas L., CAPT, USMC

6. REPORT DATE
June 1968

7a. TOTAL NO. OF PAGES
113

7b. NO. OF REFS
22

8a. CONTRACT OR GRANT NO.
N/A

b. PROJECT NO.

c.

d.

9a. ORIGINATOR'S REPORT NUMBER(S)
N/A

9b. OTHER REPORT NO(S) *(Any other numbers that may be assigned this report)*
N/A

10. DISTRIBUTION STATEMENT
This document is subject to special export controls and each transmittal to foreign nations may be made only with prior approval of the Naval Postgraduate School.

11. SUPPLEMENTARY NOTES

12. SPONSORING MILITARY ACTIVITY
Naval Postgraduate School

13. ABSTRACT
Three ion sources for the production of low energy ($E<500$ eV) ion beams have been constructed and tested for use in atomic scattering experiments. Design parameters are given for construction and operation of the sources. Two gas sources, a duoplasmatron and an electron impact source, are capable of delivering beams of H^+, H_2^+, H_3^+, He^+, N^+, and N_2^+, as well as other gas-derived ions, with beam intensities measured at a detector 75 cm downstream of $\sim 0.2\ \mu a/cm^2$. Beam currents closely parallel Langmuir-Child ($I \sim E^{3/2}$) space charge limited intensities. For the duoplasmatron, a full-width energy dispersion of 2-3% of the beam energy is observed. With hydrogen gas, beam composition of 34% H^+, 42% H_2^+, and 24% H_3^+ was achieved. Both gas sources require externally heated cathodes. The third source is a thermal device which produces lithium ion beams of $\sim 0.1\ \mu a/cm^2$ at a detector 75 cm away. The beam energy spread is a few tenths of an eV.

14 KEY WORDS	LINK A		LINK B		LINK C	
	ROLE	WT	ROLE	WT	ROLE	WT
Gas Ion Sources						
Thermal Ion Sources						
Duoplasmatron						
Electron Impact Ion Source						
Gaseous Discharge						
Energy Analysis						

thesC2738
Ion sources for the production of [redacted] en
DUDLEY KNOX LIBRARY
3 2768 00407883 2
DUDLEY KNOX LIBRARY